

Colors of Jupiter's large anticyclones and the interaction of a Tropical Red Oval with the Great Red Spot in 2008

A. Sánchez-Lavega,^{1,2} J. Legarreta,^{2,3} E. García-Melendo,^{4,5} R. Hueso,^{1,2} S. Pérez-Hoyos,^{1,2} J. M. Gómez-Forrellad,⁴ L. N. Fletcher,⁶ G. S. Orton,⁷ A. Simon-Miller,⁸ N. Chanover,⁹ P. Irwin,⁶ P. Tanga,¹⁰ and M. Cecconi¹¹

Received 5 February 2013; revised 4 November 2013; accepted 13 November 2013; published 23 December 2013.

[1] The nature and mechanisms producing the chromophore agents that provide color to the upper clouds and hazes of the atmospheres of the giant planets are largely unknown. In recent times, the changes in red coloration that have occurred in large- and medium-scale Jovian anticyclones have been particularly interesting. In late June and early July 2008, a particularly color intense tropical red oval interacted with the Great Red Spot (GRS) leading to the destruction of the tropical red oval and cloud dispersion. We present a detailed study of the tropical vortices, usually white but sometimes red, and a characterization of their color spectral signatures and dynamics. From the spectral reflectivity in methane bands we study their vertical cloud structure compared to that of the GRS and BA. Using two spectral indices we found a near correlation between anticyclones cloud top altitudes and red color. We present detailed observations of the interaction of the red oval with the GRS and model simulations of the phenomena that allow us to constrain the relative vertical extent of the vortices. We conclude that the vertical cloud structure, vertical extent, and dynamics of Jovian anticyclones are not the causes of their coloration. We propose that the red chromophore forms when background material (a compound or particles) is entrained by the vortex, transforming into red once inside the vortex due to internal conditions, exposure to ultraviolet radiation, or to the mixing of two chemical compounds that react inside the vortex, confined by a potential vorticity ring barrier.

Citation: Sánchez-Lavega, A., et al. (2013), Colors of Jupiter's large anticyclones and the interaction of a Tropical Red Oval with the Great Red Spot in 2008, *J. Geophys. Res. Planets*, 118, 2537–2557, doi:10.1002/2013JE004371.

1. Introduction

[2] Many studies have been devoted in recent times to the nature of large-scale Jovian vortices. However, their dynamics, cloud properties, and colors have not yet been fully explained (for recent reviews, see *Ingersoll et al.* [2004], *Vasavada and Showman* [2005], and *Del Genio et al.* [2009]). One way to progress in the knowledge of their properties is by studying their mutual interactions, such as those of the Great Red Spot (GRS) with other large vortices [*Sánchez-Lavega et al.*, 1998] or the mergers between vortices of similar size as former White Ovals BC, DE, and FA that led to the formation of oval

BA [*Sánchez-Lavega et al.*, 1999, 2001]. Typically, the GRS interacts directly with the abundant small anticyclones at 20°S (all latitudes in this paper are planetographic [*Sánchez-Lavega*, 2011]), forming on the poleward side of the South Equatorial Belt and move eastward [*Shetty et al.*, 2007; *Sánchez-Lavega and Gómez*, 1996; *Sánchez-Lavega et al.*, 1998]. They are engulfed by the GRS when they enter it along its eastern side [*Smith et al.*, 1979a, 1979b]. The interactions between the GRS and the large anticyclones (about a fourth of the GRS length) that form at latitudes between 21°S and 24°S are rarer. We will generically call these ovals South Tropical Ovals (acronym STrOs), although in some occasions, particular

¹Departamento Física Aplicada I, Universidad del País Vasco UPV-EHU, ETS Ingeniería, Bilbao, Spain.

²Unidad Asociada Grupo Ciencias Planetarias UPV/EHU-IAA (CSIC), Bilbao, Spain.

³Departamento de Ingeniería de Sistemas y Automática, E. U. I. T. I., Universidad del País Vasco, Bilbao, Spain.

⁴Fundació Privada Observatori Astronòmic de Catalunya Esteve Duran, Seva, Spain.

⁵Institut de Ciències de l'Espai (CSIC-IEEC), Campus UAB, Facultat de Ciències, Bellaterra, Spain.

⁶Atmospheric, Oceanic and Planetary Physics, Department of Physics, Clarendon Laboratory, University of Oxford, Oxford, UK.

⁷Jet Propulsion Laboratory, California Institute of Technology, Pasadena, California, USA.

⁸NASA-Goddard Space Flight Center, Greenbelt, Maryland, USA.

⁹Astronomy Department, New Mexico State University, Las Cruces, New Mexico, USA.

¹⁰Laboratoire Lagrange CNRS UMR 7293, Université de Sophia Antipolis, Observatoire de la Côte d'Azur, Nice, France.

¹¹Telescopio Nazionale Galileo, Roque de Los Muchachos Astronomical Observatory, Garafia, Spain.

Corresponding author: A. Sánchez-Lavega, Departamento Física Aplicada I, Universidad del País Vasco UPV-EHU, ETS Ingeniería, Alameda Urquijo s/n, ES-48013 Bilbao, Spain. (agustin.sanchez@ehu.es)

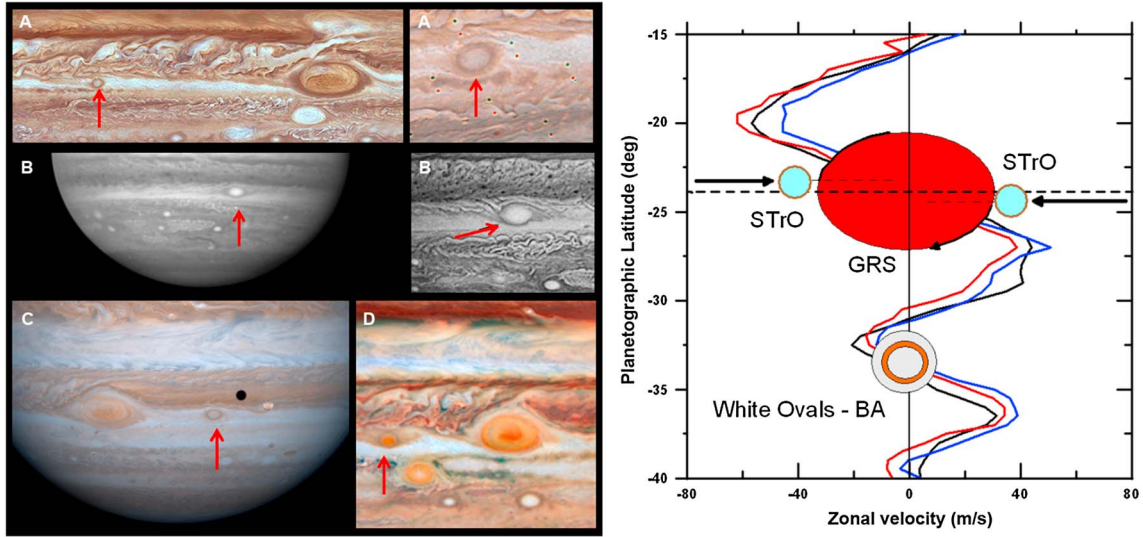


Figure 1. Selected images of (left) South Tropical Ovals (STrO) observed in Jupiter since 1979 (left) and (right) sketch of the location of the main anticyclonic ovals in the zonal wind profile [García-Melendo and Sánchez Lavega, 2001] of the southern hemisphere as measured during 1979 (Voyager data, black), 1997 (HST, blue), 2000 (Cassini, red). (a) Voyager 2 in 1979 (enlarged at right), (b) The WTrO in an HST image in 1994 (enlarged at right), (c) STrO observed by Cassini in 2000, (d) Red Oval (RO) on 9–10 May 2008 by HST. North is up and east to the right in all figures.

nicknames have been used for some of them. For example, we previously reported such an interaction between a vortex we called White Tropical Oval (WTrO) with the east side of the GRS [Sánchez-Lavega et al., 1998]. During the interaction the vortex was destroyed due to partial engulfment and ejection of its clouds by the GRS.

[3] In this paper we report an uncommon interaction between a peculiar anticyclonic red oval (we call it the Red Oval or the RO) and the GRS that occurred in June–July 2008. Since the anticyclone BA was in conjunction with the GRS, i.e., both were close to the same meridian, it was also partially involved in the interaction. Due to the similar properties of BA to those of the GRS and the RO [García-Melendo

et al., 2009; Pérez-Hoyos et al., 2009; Hueso et al., 2009; de Pater et al., 2010b; Wong et al., 2011], this event can be described as a triple-vortex dynamical interaction. Additional interest came from the strong red coloration of the RO [Strycker et al., 2011] similar to that of the red rings surrounding the GRS and BA. Thus, the study of this interaction is relevant not only for dynamical inferences on Jovian vortices but also on the nature of the red colors in Jupiter.

[4] We first describe the known properties of South Tropical Ovals on Jupiter (section 2). In section 3 we present the set of observations used in this study. Section 4 is dedicated to color characterization of these vortices and to determine, using a radiative transfer model, the cloud top altitude of the ovals. In

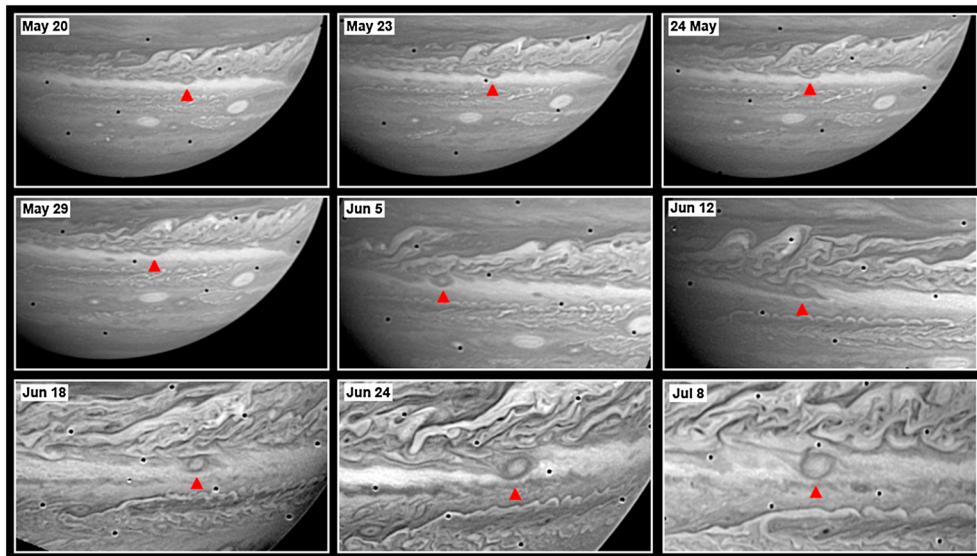


Figure 2. Sequence of Voyager 2 images in 1981 showing the formation, growth, and latitude migration of a classical STrO (indicated with a red arrow).

Table 1. Observations Summary^a

| Target | Observatory | Observing Date | Central Wavelengths (nm) |
|--------|--------------------------|-------------------------|--|
| WTrO | HST WF3 | 18 May 1994 | 218, 255, 336, 410, 439, 588, 673 |
| | HST WF3 | 15 July 1994 | 255, 336, 410, 547, 890 |
| | HST PC1 | 15 July 1994 | 255, 336, 410, 555, 890 |
| | HST PC1 | 17 July 1994 | 255, 336, 410, 555, 890 |
| RO | HST WFPC2 ^b | 9–10 May 2008 | 218, 255, 336, 410, 502, 673, 890, 953 |
| | HST WFPC2 ^c | 15 May 2008 | 255, 343, 375, 390, 410, 437, 469, 502, 673, 890 |
| | HST NICMOS ^d | 5 May 2008 | 1450, 1660, 1870, 2120 |
| | IRTF-NSFCAM ^d | 6 June 2008 | 1780, 1950, 2030, 3780, 4780 |
| | HST WFPC2 ^c | 28 June 2008 | 255, 343, 375, 390, 410, 437, 469, 502, 673, 890 |
| | HST WFPC2 ^c | 8 July 2008 | 255, 343, 375, 390, 410, 437, 469, 502, 673, 890 |
| | HST NICMOS ^d | 9 July 2008 | 1660, 1870, 2120 |
| | IRTF-NSFCAM ^d | 10 July 2008 | 1780, 1950, 2030, 2300, 3780, 4780 |
| | TNG-NICS ^d | 10 July 2008 | 1644, 1680, 2122, 2169 |
| | UKIRT-UIST ^d | 25 July 2008 | 1644, 1690, 2169, 2270 |
| | VLT-NACO ^d | 22 August 2008 | 1094, 1748, 2166, 2480 |
| | IOPW-PVOL ^d | February–September 2008 | RGB composites (~400–700 nm), 890 nm |

^aTarget: WTrO (White Tropical Oval) [see *Sánchez-Lavega et al.*, 1998]; RO (Red Oval). Observatory: The telescope and used instrument are indicated. Hubble Space Telescope (HST) with optical cameras WF/PC (WF3), WF/PC (PC1), and WFPC2, and near-infrared camera (NICMOS). Details for images are as follows:

^b*Wong et al.* [2011].

^c*Strycker et al.* [2011].

^dInfrared Telescope Facility (IRTF at Hawaii) with near infrared camera (NSFCAM); Telescopio Nazionale Galileo (TNG at La Palma, Canary I.) with adaptive near-infrared camera NICS; United Kingdom Infrared Telescope (UKIRT at Hawaii) equipped with the imaging spectrometer UIST; Very Large Telescope (VLT at ESO, Chile) with near-infrared camera NACO; International Outer Planets Watch (IOPW); and Planetary Virtual Observatory Laboratory (PVOL) imaging database. Details on the different instruments can be found at the following:

NICS: <http://www.tng.iac.es/instruments/nics/imaging.html>

AdOpt@TNG: <http://www.tng.iac.es/instruments/adopt/>

AdOpt@TNG (solar system objects): http://www.tng.iac.es/news/2007/11/09/adopt_tng/

NSFCAM: <http://irtfweb.ifa.hawaii.edu/~nsfcam/oldnsfcam.html>

NICMOS: <http://www.stsci.edu/hst/nicmos/>

http://www.stsci.edu/hst/nicmos/documents/handbooks/current_NEW/toc.html

UIST: <http://www.roe.ac.uk/ukate/projects/uist/>

NACO: <http://www.eso.org/sci/facilities/paranal/instruments/naco/overview.html>

IOPW-PVOL: <http://www.pvol.ehu.es/pvol/index.jsp?action=iopw>

Some additional images were taken from the public ALPO-Japan database web page at <http://alpo-j.asahikawa-med.ac.jp/indexE.htm>.

section 5 we describe the dynamical interaction between the RO with the GRS and BA. In section 6 we present nonlinear numerical simulations of this interaction using the nonlinear Explicit Planetary Isentropic-Coordinate (EPIC) model [Dowling *et al.*, 1998]. Finally, in section 7 we discuss the results and implications for the knowledge of Jovian vortices dynamics and their colors.

2. The South Tropical Ovals (STrOs)

[5] The South Tropical Zone of Jupiter is usually a white band at visual wavelengths extending from ~20°S to 30°S where the Great Red Spot (GRS) sits [Rogers, 1995]. It is also the place where stable and long-lived synoptic scale anticyclonic vortices (STrO) form at latitudes close to that of the GRS (lifetime ~ years, size ~5000–8000 km) (Figure 1). Most of them are isolated and destroyed by the GRS after encountering it [see, e.g., *Sánchez-Lavega et al.*, 1998]. STrOs are usually “white” ovals with an albedo similar to that of the South Tropical Zone, enclosed by a dark, low-albedo ring that outlines their border. STrOs can be distinguished clearly from the smaller series of anticyclones that form in strings at latitude 20°S in the southern border of the South Equatorial Belt (SEB), because of the larger sizes of typical STrOs. They are also isolated and separated ~2° in latitude from the SEB edge. For a general overview of the properties and models of Jovian vortices, see *Ingersoll et al.* [2004].

[6] Ground-based imaging records supported by occasional spacecraft observations show that there have been about seven STrO vortices in Jupiter between 1983 and 2008 (Figure 1). The first case was the White Tropical Oval (WTrO) that formed in 1983 and ended following a GRS encounter in 1997 [Sánchez-Lavega *et al.*, 1998]. Having been observed with some detail with the Hubble Space Telescope, it is considered for further study in this paper. A second one was present during the Cassini flyby of Jupiter in 2000 and was similar in its morphology to the WTrO. Between 2002 and 2007 there were about four different STrOs according to ground-based imaging. The last oval formed during the Sun-Jupiter conjunction in 2008. It was first detected in ground-based images in February 2008, and it was remarkable because it showed a pronounced red color [de Pater *et al.*, 2010b; Strycker *et al.*, 2011]. This Red Oval (RO) was accompanied by another similar oval about 60° apart in longitude but “white” in color, providing the puzzle of color dichotomy between similar ovals despite their occurrence at the same latitude and time. The RO vortex attracted the attention of researchers because of its intense red color, a property whose nature (coloring agent and its origin) is so far unknown. It is important to distinguish the RO from oval BA, this last one is sometimes also nicknamed “red oval” because of the variable reddening of an internal ring inside it [Simon-Miller *et al.*, 2006; Pérez-Hoyos *et al.*, 2009; Shetty and Marcus, 2010; Wong *et al.*, 2011].

[7] The South Tropical Ovals form when the South Equatorial Belt (SEB) is in its classic “belt” state, i.e., when

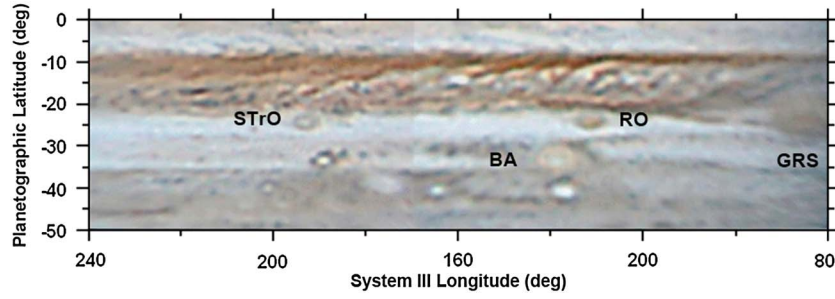


Figure 3. Cylindrical map of Jupiter obtained from IOPW-PVOL images contributed by A. Wesley on 14 March 2008 showing early images of the Red Oval (RO) and a STrO companion. Each image is a RGB color composite showing approximate Jovian features colors. Other vortices are also identified.

it shows a dark albedo at visual wavelengths and the belt is active, with plenty of turbulence in its interior [Sánchez-Lavega and Gómez, 1996]. In this stage, series of small spots form along the SEB southern edge at 19°S , apparently when the eastward jet at this latitude becomes unstable (Figure 1). Image sequences taken by the Voyager 1 and 2 spacecraft in 1979 [Smith *et al.*, 1979a, 1979b] and more recently those taken at high resolution by ground-based telescopes have shown that a STrO forms from these small anticyclones. Typically, when two of them meet, they form a mutual pair, circulating around one another and ultimately merging to generate a larger vortex (a STrO) that migrates slightly southward in latitude by about 2° into the South Tropical Zone (STrZ) (Figure 2). On other occasions, a larger oval at the SEB border grows by absorbing surrounding material and separates slightly from the belt and penetrates into the STrZ, near latitude 23°S where the velocity of the zonal wind is close to zero (Figure 2). No STrOs are observed to form during the SEB Fade stages of the belt. Since the STrO slightly differ in latitude from the GRS, they show a small longitudinal relative drift, encountering with the GRS at a

time that depends on the relative velocity of both features and their initial separation in longitude (Figure 1). Their encounter represents the end of the STrO, as was observed with the WTrO [Sánchez-Lavega *et al.*, 1998] and with the RO (this work).

3. Observations and Analysis

[8] This study is based on different sets of observations obtained with a variety of instruments. Although the main objective was the study of the RO, we also do a reanalysis of the spectral reflectivity of the WTrO in order to compare it with the RO measurements. Table 1 summarizes the observations used in this paper.

[9] The study of the long-term evolution and interaction of the RO with the GRS and BA was based on the analysis of about 150 color composite images (wavelength range from ~ 400 to 700 nm), from the International Outer Planets Watch-Planetary Virtual Observatory and Laboratory (IOPW-PVOL) imaging database [Hueso *et al.*, 2010] which covered the period February–September 2008. Typically, telescopes

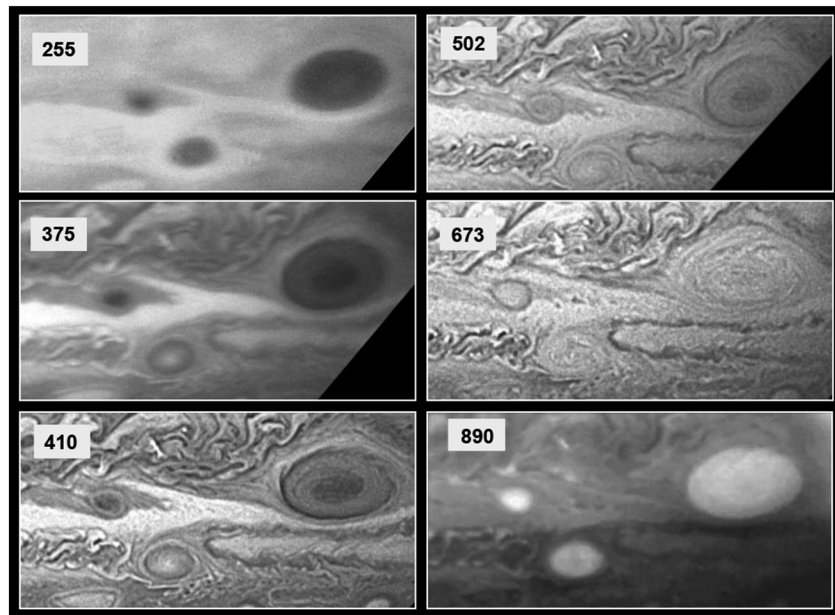


Figure 4. The three ovals (GRS, BA, and RO) as they were seen before their mutual interaction on 15 May 2008 at selected wavelengths (indicated in nm) on HST images.

Table 2. Main Vortices Properties

| Vortex | Latitude (ϕ_g) | Length N-S | Length E-W | $\omega_{\text{System III}}$ ($^\circ/\text{d}$) | u (m s^{-1}) | Peak Tangential Velocity | Mean Vorticity | Reference |
|-------------------|-----------------------------|----------------------------|----------------------------|--|---------------------------|--------------------------|-------------------------------------|-------------------------------------|
| BA | $-33.1^\circ \pm 0.5^\circ$ | $6.4^\circ \pm 0.5^\circ$ | $8.3^\circ \pm 0.5^\circ$ | -0.2 | $+1.3$ | 110 m s^{-1} | $2.9 \times 10^{-5} \text{ s}^{-1}$ | Hueso <i>et al.</i> [2009] |
| RO | $-24.2^\circ \pm 0.4^\circ$ | $3.4^\circ \pm 0.5^\circ$ | $4.8^\circ \pm 0.5^\circ$ | $+0.04$ | -0.3 | 45 m s^{-1} | $2.1 \times 10^{-5} \text{ s}^{-1}$ | This work |
| WTrO | $-21.5^\circ \pm 0.5^\circ$ | $4.1^\circ \pm 0.3^\circ$ | $7.0^\circ \pm 0.6^\circ$ | $+0.6$ | -4 | 40 m s^{-1} | $1.3 \times 10^{-5} \text{ s}^{-1}$ | Sánchez-Lavega <i>et al.</i> [1998] |
| STrO ^a | $-23.3^\circ \pm 0.5^\circ$ | $3.8^\circ \pm 0.5^\circ$ | $4.4^\circ \pm 0.5^\circ$ | $+0.4$ | -3 | 50 m s^{-1} | $2.2 \times 10^{-5} \text{ s}^{-1}$ | This work |
| GRS | $-22.7^\circ \pm 0.4^\circ$ | $11.1^\circ \pm 0.5^\circ$ | $17.1^\circ \pm 0.5^\circ$ | $+0.3$ | -1.95 | 120 m s^{-1} | $1.4 \times 10^{-5} \text{ s}^{-1}$ | Sada <i>et al.</i> [1996] |

^aThis STrO is that on Cassini flyby images (Figures 1c and 4a).

with apertures in the range 25–40 cm were used for those observations. Each RGB (R: red, G: green, B: blue) image was generated from a video record of the planet through a color filter at typical rates of 30 frames per second. A single one-filter image is formed after recentering of selected frames according to their quality that are added to form a single improved image using the “lucky imaging” technique [e.g., Law *et al.*, 2006]. Each single image frames is then processed for contrast enhancement using a wavelet filter method, being RegiStax [Berrevoets *et al.*, 2011] the most common software used by the IOPW team for these procedures. Image navigation (orientation and limb determination) and position measurement (pointing on a target with pixel coordinates transformed to planetary coordinates) were done with the software Laboratorio Analisis Imagenes Astronomicas (LAIA) [Cano, 1998].

[10] Additionally, we used selected sets of unprocessed images taken by some members of the IOPW team using a narrow-band methane-absorbing filter centered at a wavelength of 890 nm to obtain photometric data for cloud top retrieval (see section 6.1).

[11] The second set of images was obtained with the Hubble Space Telescope (HST) Wide Field Planetary Camera 2 (WFPC2). They were obtained using an extensive set of filters covering the spectral range from 210 nm to 953 nm (Table 1), and we used them to study the RO properties at visual wavelengths. The spectral reflectivity of the previously studied long-lived WTrO [Sánchez-Lavega *et al.*, 1998] was also obtained from a selected set of HST images taken in 1994 in

three runs with the former Planetary Camera in modes WF/PC (WF3) and WF/PC (PC1). These images were navigated using the software LAIA and those used for cloud tracking were processed by means of a standard contrast enhancement filter incorporated in LAIA. Their photometric analysis is described in sections 5 and 6.1.

[12] The third set corresponds to the near-infrared wavelength range ($\sim 1\text{--}5.0 \mu\text{m}$) for which we used images obtained with the following telescopes and instruments (see Table 1 and its footnotes for links to instrument description): (1) 3.58 m Telescopio Nazionale Galileo (TNG) at the Roque de los Muchachos Observatory (La Palma, Canary Islands), using the Near Infrared Camera Spectrometer (NICS), which covered a wavelength range from 1.66 to 2.169 μm at two different spatial resolutions. The adaptive optics module (AdOpt) on this instrument provides images with maximum angular resolution of 0.08 arcsec/pixel (0.04 arcsec/pixel) over a $1.4' \times 1.4'$ ($0.7' \times 0.7'$) field. In our observations we used the satellite Io as a wavefront guide and a closed looping sequence satellite-planet with a 200 Hz correction cycle. For details on this module, wavefront sensing, tip/tilt operation, and examples of its use for solar system objects, see link in Table 1 footnotes. (2) The 3.0 m NASA Infrared Telescope Facility (IRTF) at Mauna Kea, Hawaii) equipped with the NSFCam camera, which covered a wavelength range from 1 to 5.5 μm providing a maximum resolution of 0.3 arcsec/pixel, (0.15 arcsec/pixel and 0.06 arcsec/pixel) with a corresponding field of view of 76.8" (37.9" and 14.1"), respectively. (3) The 2.4 m Hubble

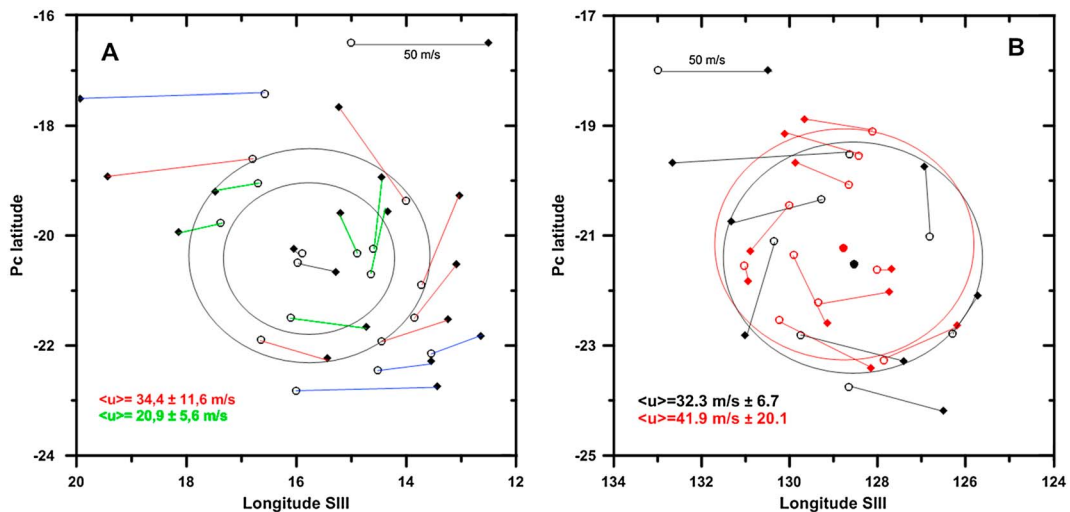


Figure 5. Maps showing the vortices contours and the displacements of cloud features around them in image pairs separated by 10 h for (a) the STrO observed by Cassini in 2000 and (b) the Red Oval RO observed by HST in 2008. The motions of features at similar distances from the center are identified by lines with the same colors.

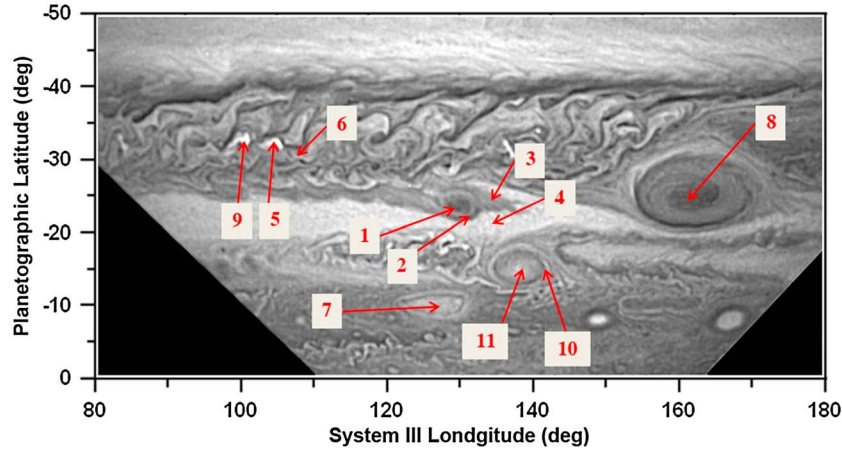


Figure 6. Identification of the features selected to retrieve the spectral relative reflectivity (image by HST on 15 May 2008 at a wavelength of 410 nm): (1) RO center; (2) RO ring; (3) RO background; (4) STrZ reference area; (5) storm 1; (6) SEB; (7) cyclone; (8) GRS center; (9) storm 2; (10) BA ring; and (11) BA center.

Space Telescope-Near Infrared Camera and Multi-Object Spectrometer (NICMOS) provided images covering the wavelength range from 0.8 to 2.5 μm . We used the cameras NIC1 (providing 0.043 arcsec/pixel with diffraction-limited wavelength at 1 μm) and NIC2 (providing 0.075 arcsec/pixel with diffraction-limited wavelength at 1.72 μm). (4) The 3.8 m United Kingdom Infrared Telescope (UKIRT at Hawaii) equipped with the imaging spectrometer UIST in the spectral range 1.58–2.30 μm provided images with an angular resolution 0.12 arcsec/pixel (0.06 arcsec/pixel) over a $2' \times 2'$ ($1' \times 1'$) field, respectively, again for the different magnifications available. (5) Very Large Telescope (VLT) operated by European Southern Observatory (ESO) at Chile used the Yepun (UT4) 8.2 m telescope with NAOS-CONICA (NACO) instrument at the Nasmyth-Focus B, which is an Adaptive Optics imaging facility (Nasmyth Adaptive Optics System (NAOS)) covering the near-infrared spectral range up to 2.5 μm (field of view 56×56 arc sec at 0.054 arcsec/pixel). It works guiding on a natural star or in an artificial sodium laser guide star and has two wavefront sensors (visible and infrared), the infrared one operating in the range (0.8–2.5 μm). The Jupiter observations with NACO at the VTL were performed with the adaptive optics (AO) locked on Io, with a distance to the planet ranging from $42''$ to $23''$. The AO correction was perfect: images full width at half maximum at 2.12 microns were <3 pixels, with Strehl ratio measured (on axis) by the Wavefront Fourier Sensing (WFS)=60–70%. At Jupiter's distance this translates into a physical resolution of ~ 400 km, and the series of images were obtained with an excellent S/N ratio (>5 for faint features). Details on the operation of this instrument can be found in the link in Table 1 footnotes. Their image navigation and mapping was done using the software LAIA. The photometric flattening of those used for the spectral brightness measurement is described in sections 5 and 6.1, with further details given in *Barrado-Izaguirre et al.* [2013]. Because of variable seeing conditions and ample number of wavelengths used in this third set of ground-based images, their typical resolution is in the range ~ 0.2 – 0.5 arcsec/pixel. Because of the variable distance to Jupiter, telescopes and wavelengths used, the standard resolution (at the Red Oval latitude in central meridian) provided by HST images is in the range ~ 300 – 500 km and ~ 400 – 1500 km for ground-based telescopes.

4. Red Oval Properties

[13] The RO was observed for the first time in February 2008 following the Jupiter-Sun conjunction when it was close to BA's longitude (Figure 3). We use System III longitudes along the whole work [Sánchez-Lavega, 2011]. Its formation was therefore not observed, but we can imagine an origin sim-

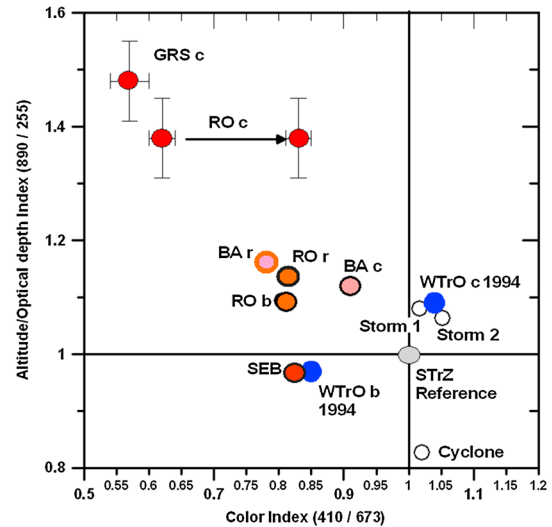


Figure 7. Diagram showing the indices CI and AOI for different Jovian features in two epochs (1994 and 2008). For 2008 (see feature identifications in Figure 5): GRS center (GRSc), Red Oval center (ROc), RO background (ROb), BA center (BAc), BA ring (BAr), storms 1 and 2, SEB, and cyclone. For 1994 White Tropical Oval center and background clouds (WTrOc, WTrOb). For ROc the arrow marks the change in color before its interaction with GRS-BA at left (15 May 2008) and following the interaction at right (8 July 2008). To make the figure simpler, the index error bars are shown only for the GRSc (mean from measurements on 9 and 15 May, 28 June, and 8 July 2008), ROc before interaction with GRS (9 and 15 May, and 28 June, left point), and ROc following its interaction with GRS and BA (8 July 2008).

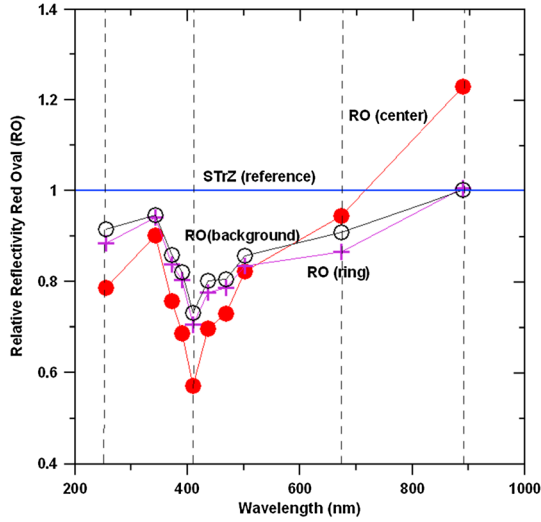


Figure 8. Coarse spectra of the Red Oval reflectivity relative to a STrZ reference area (15 May 2008). Three regions are shown: the RO center (the red area, solid red dots), the RO ring (crosses), and the RO background patch of clouds where the RO sits (empty circles; see Figure 5).

ilar to that of other STrOs as described above, as the SEB was prior to the solar conjunction very active in spot development with its classical disturbed morphology. The RO was accompanied by another STrO placed about 60° west of it and at the same latitude but it was “white” in color.

[14] The RO cloud morphology at different wavelengths can be seen in Figure 4 (compare to *de Pater et al.* [2010b, Figures 3, 5, and 13]). The RO is placed within the high-albedo South Tropical Zone but surrounded by a patch of lower albedo clouds. The Red Oval consisted of an outer ring (high albedo at 410 nm, dark at 673 nm) that enclosed an area of uniform reflectivity. Its size was 5500 km in the east-west direction and 4175 km in the north-south meridional direction, while the outer ring thickness was of 575 ± 115 km (Table 2). Note that the outer ring is a common characteristic of the STrO as shown in Figure 1.

[15] We were able to track the rotation of some features about the center of the RO in pairs of images separated by one planetary rotation, retrieving the wind tangential velocity [*Legarreta and Sánchez-Lavega*, 2005]. For a comparison with other STrO we also measured the rotation of the STrO observed during the Cassini flyby in 2000 (Figure 1c). As shown in Figure 5, both vortices showed similar rotation properties: (a) They have anticyclonic rotation; (b) the peak tangential velocity at oval periphery is $V_T = 40\text{--}50$ m s $^{-1}$; and (c) the few available data indicate that the velocity decreases toward the center. The peak vorticity is given by

$$\zeta_{\text{peak}} = \frac{\int_C \vec{V}_T \cdot d\vec{\ell}}{\text{Area}} \approx \frac{V_T L_e}{\pi a b} = \frac{2V_T}{b} \left[1 - \frac{e^2}{4} - \frac{9e^4}{192} - \dots \right] \quad (1)$$

where for simplicity, the oval is assumed to be an ellipse with semiaxis a , b , perimeter L_e , and eccentricity e . Since we assumed a constant value for V_T along the integration path, the value of the circulation is $V_T L_e$. Table 2 gives the peak vorticity for all the ovals we measured here showing that they are quite similar. The similar values to those for RO were found

for the Cassini STrO and for the WTrO [*Sánchez-Lavega et al.*, 1998], confirming that the STrO vortices have similar sizes and rotation speeds. Being of different colors, this result indicates that color is not related to vortex strength or horizontal circulation. In Table 2 we also show that the drift in longitude of the RO and the GRS differed slightly by $\sim 0.25^\circ/\text{d}$, which translates in a relative speed of ~ 1.5 m s $^{-1}$, i.e., both ovals slowly approached one another.

5. Color Characterization

[16] *Strycker et al.* [2011] give a comprehensive introductory review to the color characterization in Jupiter. In essence, the absolute spectral reflectivity $I/F(\lambda)$ that varies across the disk (longitude and latitude) and depends on the viewing geometry (phase angle) is determined by radiative processes in the gas (scattering and absorption) and in the particles, depending on their vertical distribution [*West et al.*, 2004]. The coloration we see depends on a combined effect of these processes. Different techniques have been employed to characterize colors and look for the chromophore agents on the Jovian atmosphere in terms of its spatial distribution, such as the cluster analysis method [*Thompson*, 1990], and the principal component analysis or PCA [*Simon-Miller et al.*, 2001a, 2001b; *Dyudina et al.*, 2001]. Here we follow a different simpler approach consisting on a relative photometry measurement of the features and the introduction of two photometric indices to characterize and compare the color and the adaptive optics properties of selected Jovian features in comparison to those of the Red Oval.

[17] In Figure 4 we show images of the RO, the GRS, and BA taken with a set of filters covering the spectral wavelength range from 255 to 890 nm. The three ovals are dark at ultraviolet wavelengths (255 nm) due to the strong absorption by high-altitude haze particles, but bright in the methane

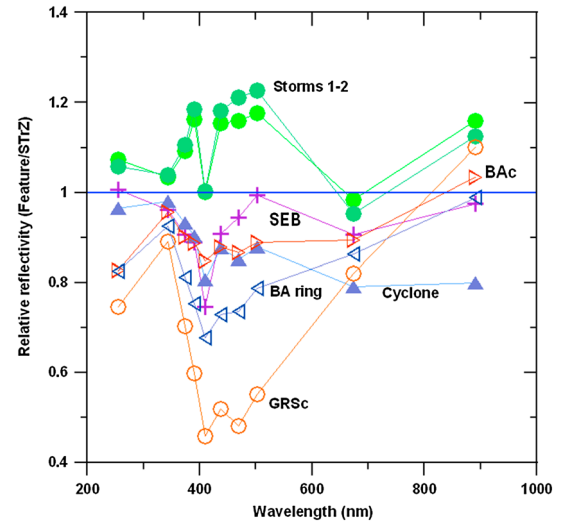


Figure 9. Spectral reflectivity of different Jovian features in the region of the Red Oval on 15 May 2008 (see Figure 5 for identification) relative to a reference area in the STrZ. The features are storms 1 and 2 (convective in SEB, solid green dots), SEB (crosses), GRS center (GRSc, empty orange circles), BA center (BAc, empty orange triangles) and ring (BAr, empty blue triangles), and cyclone (solid violet triangle).

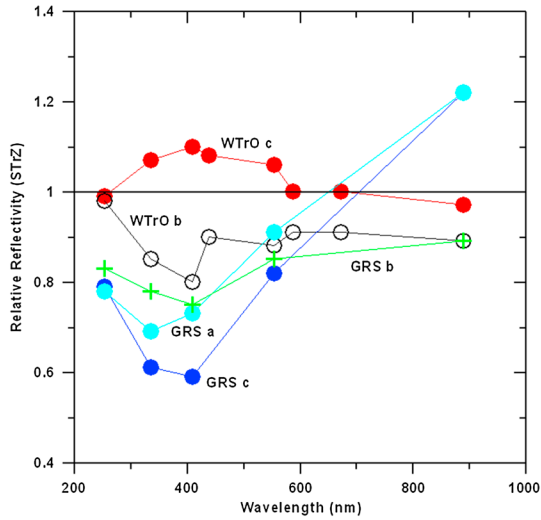


Figure 10. Spectral reflectivity of the GRS and White Tropical Oval (WTrO) in May and July 1994. The spectra are for the GRS center (GRSc, solid dark blue circles), GRS surrounding clouds (GRSb, green crosses), the area in the GRS outside its center (between its periphery and central region, GRSa, solid cyan circles), the WTrO center (WTrOc, solid red circles), and its surrounding area (WTrOb, empty black circles).

absorption band at 890 nm, since their cloud or haze tops are located high in the atmosphere as discussed below. Color composites show the RO to be as red as the GRS (see also inset in Figure 15 and *de Pater et al.* [2010b, Figures 5 and 13]).

[18] We have characterized the colors of different Jovian features in the region of the vortex by performing relative photometry at all the wavelengths available on HST images (Figure 6). This is the same set of images employed by *Strycker et al.* [2011], where absolute photometry data can be found. We used the software LAIA [*Cano, 1998*] to retrieve the reflectivity in uncalibrated *Digital Number (DN)* (counts) of the Jovian features we consider in this study. We took as a photometric reference for normalization an area in the STz close to the location of the features of interest with the same area as that occupied by the targets. Relative reflectivity highlights the spectral differences between features more effectively than, for example, direct comparison of absolute reflectivity spectra.

[19] *DN* counts were retrieved for a disk with a size of 0.4 arcsec on each feature at each wavelength, and then the mean value was divided by the cosine of the viewing angle μ_0 (which is equivalent to assuming that the features behave as Lambert reflectors). To get an idea of the disk size we employed, note that the RO typically extends about 25 pixels

or 1.2 arc sec. Errors in the average *DN*s (total value divided by the pixel area) come from the *DN* variability within the area and were typically of the order of 2–5%. Additionally, area pointing and image navigation (determination of the planetary limb) account for errors that translate the uncertainty in *DN* to less than 10%. Larger errors are present in the images taken with the 890 nm methane band filter because of vignetting of the HST field of view [*Karkoschka and Koekemoer, 2002*]. For this reason, measurements close to the edge of the field were avoided as much as possible. However, when a feature was in this nonuniform area, we corrected its reflectivity using a simple linear interpolation from the center to the border of the field reflectivity profile. We estimated relative photometry errors with this filter to be around 15%. The relative reflectivity of a feature at a given wavelength is then given by

$$R_k(\lambda) = \frac{\langle DN(\lambda) \rangle_k / \mu_{0k}}{\langle DN(\lambda) \rangle_4 / \mu_{04}} \quad (2)$$

where the index k denotes the value for the feature and subindex 4 is used for the STz reference area according to Figure 6.

[20] By using this procedure, we have measured the reflectivity of selected features in the HST image series corresponding to two periods: (1) GRS-RO-BA interaction in 2008. This corresponds to dates 15 May (pre-GRS-RO interaction), 28 June (beginning of the GRS-RO interaction), and 8 July (post-GRS-RO interaction); and (2) the WTrO in 1994. For comparison purposes, we also reanalyzed the HST images of the White Tropical Oval (WTrO) and the GRS taken in 1994. It must be noted that the WTrO showed, along its lifetime, transient color changes (from white to reddish) as discussed in *Sánchez-Lavega et al.* [1998] (see also *Morales-Juberias et al.* [2002] for anticyclone properties in this period).

[21] We obtain a quantitative characterization of color by introducing two indices based on four filters from the HST observations. These are a color index (CI) and an altitude-opacity index (AOI), defined respectively as

$$CI_k = \frac{R_k(\lambda = 410 \text{ nm})}{R_k(\lambda = 673 \text{ nm})} \quad (3)$$

$$AOI_k = \frac{R_k(\lambda = 890 \text{ nm})}{R_k(\lambda = 255 \text{ nm})} \quad (4)$$

[22] The first index is sensitive to the color of a given feature since an abrupt change in the spectral reflectivity profile occurs in Jupiter between the two wavelengths: blue (410 nm) and red (673 nm) [*Karkoschka, 1998*]. The reflectivity values are taken

Table 3. The 890 nm Methane Band Absolute Photometry

| Observer ^a | Date | GRS | | | BA | | | RO | | |
|-----------------------|------------|-------|---------|------|-------|---------|------|-------|---------|------|
| | | μ | μ_0 | I/F | μ | μ_0 | I/F | μ | μ_0 | I/F |
| D. Parker | 2008/06/03 | 0.920 | 0.887 | 0.15 | 0.881 | 0.878 | 0.12 | 0.927 | 0.942 | 0.12 |
| D. Parker | 2008/06/20 | 0.941 | 0.945 | 0.15 | 0.859 | 0.869 | 0.12 | 0.875 | 0.897 | 0.12 |
| B. Gahrken | 2008/06/29 | 0.822 | 0.804 | 0.18 | 0.766 | 0.750 | 0.12 | 0.889 | 0.878 | 0.12 |
| D. Peach | 2008/07/01 | 0.851 | 0.864 | 0.15 | 0.790 | 0.802 | 0.11 | 0.748 | 0.765 | 0.09 |
| C. Go | 2008/07/07 | 0.925 | 0.926 | 0.14 | 0.867 | 0.868 | 0.09 | 0.930 | 0.931 | 0.11 |

^aFrom methane band imaging by IOPW observers.

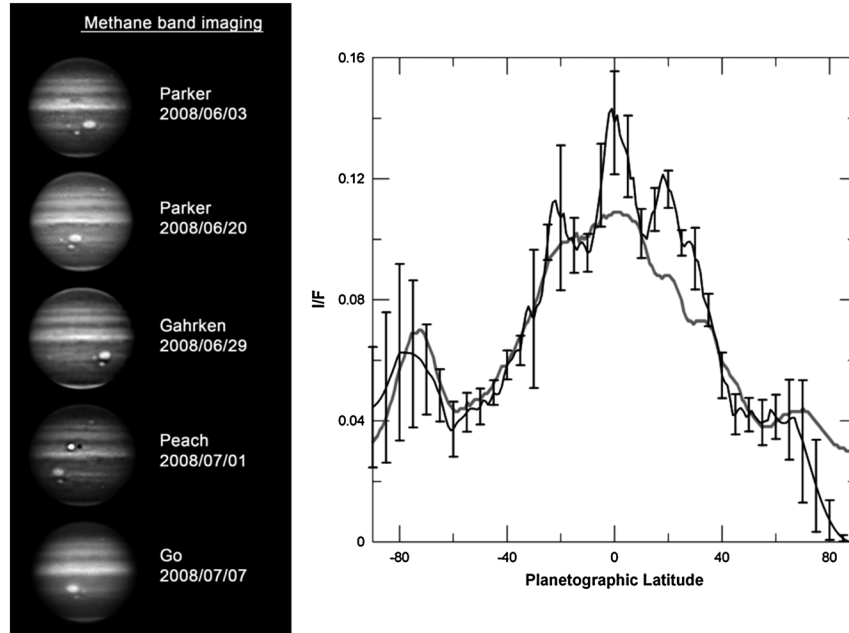


Figure 11. (left) Sample of 890 nm methane band images from IOPW used for photometry and cloud top altitude determination. The three ovals (GRS, BA, and RO) stand out by their brightness. (right) North-south averaged 890 nm reflectivity with error bars indicated for the above images (dark line), and the HST reference profile for calibration (grey line) [Chanover *et al.*, 1996]. Dates and names of IOPW-PVOL and ALPO-Japan observers are indicated. South is up and east to the left.

relative to a uniform area in the STrZ. Filters with wavelengths close to these can also be used as a color index. For example, *de Pater et al.* [2010b] and *Wong et al.* [2011] used a similar index, defined as $1 - (F435N/F658N)$ to create images they call “chromophore” (or color) with these numbers corresponding to the HST blue (F435) and red (F658) filters. We found that in Jupiter, the CI index runs from about 0.5 for red features (GRS, RO) to about 1.1 for the “white” (spectrally flat) features, as seen in RGB composites; the index $CI=1$ for the STrZ area is used as a reference.

[23] The second index is sensitive to the upper haze altitude-optical depth (in the methane absorption band at 890 nm) and its ultraviolet opacity at 255 nm. We found that AOI runs from 0.8 for features with a low altitude and UV optically thin upper haze (typically for cyclones) to 1.5 for high altitude and UV thick upper hazes (for anticyclones). A typical separation limit in altitude for high and low hazes is around the tropopause (~ 100 mbar).

[24] Figure 7 shows a two-index diagram representation that serves as simple classification of the spectral reflectivity of usual Jovian features, including some of the anticyclones under study in this work. This figure shows many characteristic aspects of the known colors and top altitudes for Jovian features, but more importantly, it shows the extremely different behavior between the WTrO (1994) and the RO (2008). It also shows that the ring of BA is not as red as the center of the RO and the GRS but is very similar to the ring of the RO and the background clouds that surround it. Finally, we show the change in the index CI for the center of the RO (ROc) before its interaction with the GRS (9 and 15 May and 28 June) and following it (8 July 2008). Accordingly, the RO lost part of its red coloration after interaction, but the AOI (and therefore, its vertical structure) did not change significantly. A plausible

interpretation is that following the interaction, and as soon as the RO was broken, its top upper haze preserved its altitude but at the same time decreased its red coloration because of the change that occurred in its dynamical properties, or simply because of mixing with surrounding material (see the dynamical analysis below).

[25] Figure 8 shows the relative spectral reflectivity of the RO and its surroundings. It is obvious that the vortex center, ring, and background area have a similar behavior with a pronounced deep minimum in reflectivity at 410 nm. The RO center (the red region) shows the deeper absorption at 410 nm, and globally, a lower reflectivity at all the wavelengths except at 890 nm, indicating that its central area is elevated relative to its surroundings.

[26] In Figure 9 we show the relative spectral reflectivity for some selected features indicated in Figure 6. It is interesting to note that the deep minimum at 410 nm is present in all the features. It is broader and deeper in the case of the GRS but also notable in the ring of Oval BA. These two features (GRS and BA ring) show a spectral behavior similar to that of the RO but with a different intensity of the red signature. However, the spectra of the other features differ from that of RO and GRS. The cases of the convective storms (storms 1 and 2) and the cyclone are particularly noteworthy. It seems evident that the red color intensity is mostly linked to the absorption intensity around the 410 nm wavelength (see also *Simon-Miller et al.* [2006] and *de Pater et al.* [2010b]).

[27] In Figure 10 we show the spectral reflectivity of the GRS and the WTrO as measured in 1994. Whereas the spectrum of the GRS follows that of 2008 with the characteristic minimum in reflectivity at 410 nm, the WTrO spectrum differs markedly from that of the RO. Globally, the reflectivity of the WTrO is above or similar to that of the STrZ,

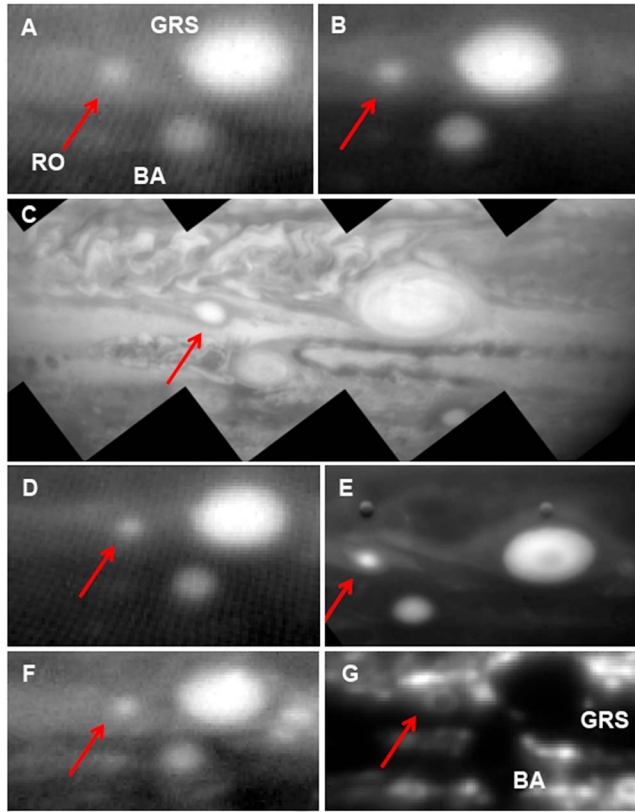


Figure 12. Spectral images in the near infrared of the three anticyclones before their interaction. They are identified with the Red Oval (RO) marked with an arrow in all the image subsets. The wavelengths (in microns) are (a) 1.78, (b) 1.95, (c) 1.87, (d) 2.03, (e) 2.12, (f) 3.78, and (g) 4.78. The used instruments and dates are IRTF-NSFCAM on 16 June 2008 for Figures 12a, 12b, 12d, 12f and 12g and HST-NICMOS on 16 May 2008 for Figures 12c and 12e.

whereas that of the RO was always lower except at 890 nm. The 410 nm absorption is absent in the WTrO central region, although a sign of it is seen in the background low-albedo area where the WTrO sits (see Figure 1b). The WTrO reflectivity at 255 nm and 890 nm is similar to that of the STrZ but opposite to what we observed in the RO, which showed higher values than the STrZ. Thus, we conclude that although both anticyclones are equivalent in their latitude location, background winds, and dynamics, their colors differ markedly.

6. Vortices Cloud Top Altitudes

[28] Previous works have partially addressed the vertical cloud structure of anticyclone vortices and serve as a reference for our calculations. *Banfield et al.* [1998] presented radiative transfer models of the cloud vertical structure for the GRS and White Ovals using Galileo visible images. *Strycker et al.* [2011] presented similar models for the three ovals GRS, BA, and RO based on the images taken with the HST in 2008 in the 255–673 nm spectral range. Detailed models for BA before and after its red coloration change were presented by *Pérez-Hoyos et al.* [2009]. Later, *de Pater et al.* [2010b] presented oval models based on 1–1.65 μm spectra, and *Wong et al.* [2011] used long-term methane band imaging at 890 nm to constrain the changes in the top altitude of the upper haze of BA. Combining the results of these studies, the

following vertical haze and cloud structure can be assumed: (1) an uppermost haze layer located in the stratosphere which extends from 1 to the 100 mbar level, absorbent in the UV with an optical depth ranging from $\tau \sim 0.5$ to 0.05 from wavelengths 255 nm to 890 nm ($\tau \sim 0.11$ –0.15 at 502 nm); (2) a dense tropospheric haze extending between pressure levels ~ 100 –700 mbar with an optical depth $\tau \sim 2$ –5 in the visible wavelength range, with a wavelength dependent single scattering albedo $\varpi_0(\lambda)$ for the particles according to *Strycker et al.* [2011]; (3) an optically thick cloud with $\tau > 20$ and top at 400–700 mbar at the top of the ammonia condensation level. Differences in these parameters within a given layer produce the reflectivity differences we see between the three vortices. We employ these results to constrain, by means of a simple radiative transfer model, the vortices' cloud and haze vertical structure from our reflectivity measurements in the 890 nm methane band and in the near-infrared wavelength range (1.7–2.3 μm).

6.1. Photometry in Absorption Bands From 0.89 to 2.3 μm

[29] Photometry of images obtained with an 890 nm methane band filter by IOPW observers is given in Table 3 and Figure 11. This filter is particularly well suited to control the changes in the tropospheric haze layer because for an absorption coefficient of $20 \text{ (km amagat)}^{-1}$, a representative value for the filters used by the observers given in Table 3,

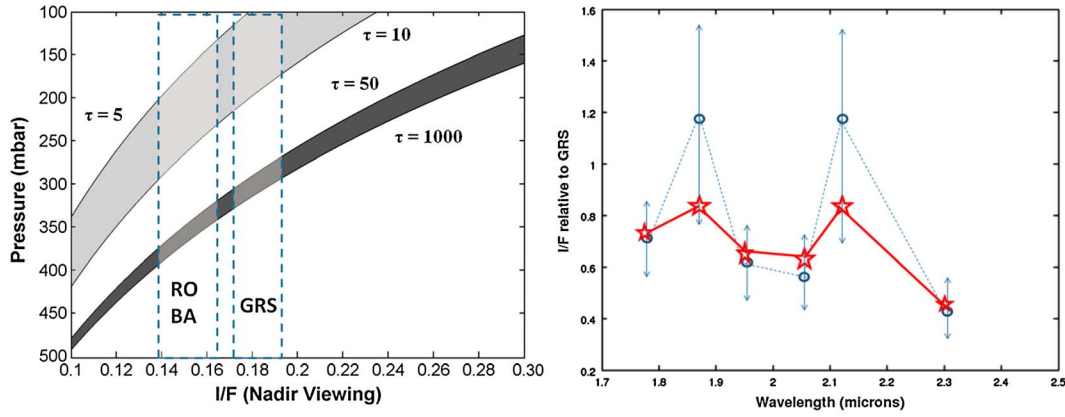


Figure 13. (left) Model results of the reflectivity at the 890 nm methane absorption band as a function of the altitude level of the main cloud layer (assumed to be an isotropic layer with $\omega_0 = 0.95$) and for different optical depths (τ) grouped in two cases: $\tau = 5$ –10 and $\tau = 50$ –1000. The observed reflectivity range for GRS, BA, and RO is indicated. (right) Comparison between the observed (blue) and modeled (red) relative spectral reflectivity of the Red Oval relative to that of the Great Red Spot in the 1.7–2.3 μm wavelength range. The model-measurement deviations seen at 1.86 and 2.12 μm are due to a systematic calibration error in NICMOS images.

the pressure at which the gas absorption optical depth is 1 is reached at 540 mbar [see, e.g., *Sánchez-Lavega*, 2011]. For a standard haze-cloud Jovian model [*West et al.*, 2004], this level moves upward in the atmosphere, closer to the tropopause level [*de Pater et al.*, 2010a]. For this study we have avoided the use of the HST 890 nm methane band images because of the nonuniformity in radiance at the edges in the field of view with the FQCH4P15 filter.

[30] The IOPW images were navigated using the LAIA software [*Cano*, 1998]. The intensity calibration was performed by reference to methane band imaging with HST published by *Chanover et al.* [1996]. For this purpose, we computed the DN to I/F factor required to transform north to south scans along the central meridian to the values retrieved by *Chanover et al.* [1996]. This assumes no overall change in Jupiter's reflectivity at this band. Figure 11 shows the average reflectivity of all IOPW observations and their standard deviation (black line) in a north-south scan compared to the HST reference profile (solid grey line). The standard deviation provides a reasonable error bar for reflectivity values in Table 3, which amounts up to a 10% (± 0.01 in I/F).

[31] The dependence of the reflectivity at 890 nm with the cosine of the incident angle (μ) and in the cosine of the emission angle (μ_0) was corrected by using the following law:

$$(I/F)_{\text{corr}} = (I/F)_{\text{obs}} / \mu \mu_0 \quad (5)$$

[32] After this correction, we observed that the GRS was slightly brighter than the other two ovals, whose reflectivity was similar (Table 3). Our data for BA compare very well with long-term measurements given by *Wong et al.* [2011, Figures 5 and 6], validating the photometry retrieved for the other vortices. A comparison with *de Pater et al.* [2010b] shows that GRS looks brighter in our results. This is because of the use of filters with various widths at a relatively narrow absorption band and also because of the geometrical correction used in each case. On the other hand,

reflectivity ratios between GRS and BA are in good agreement. One result we get is a relatively constant value for the reflectivity at the methane band wavelength for the three vortices before, during, and after their mutual interaction, with $I/F = 0.18 \pm 0.02$ (GRS), 0.15 ± 0.02 (BA), and 0.15 ± 0.01 (RO).

[33] The appearance of the vortices in the near infrared (1–5 μm) is shown in Figure 12. The spectral range 1.78–2.30 μm is dominated by the methane absorption bands and the molecular hydrogen band, particularly at 2.12 μm [*Borysow*, 2002]. The optical depth $\tau = 1$ is reached at an altitude level ranging from $P \sim 10$ to 100 mbar for these methane bands [*West et al.*, 2004]. Thus, images in this spectral range mostly show the vortices as bright ovals, since sunlight is reflected at their topmost high-altitude haze layer (Figures 12a–12f). Recently, *de Pater et al.* [2010b, 2011] presented models for the GRS, BA red ring, and a northern red oval from reflectivity in this spectral range that fits to a model that includes three layers with particles (stratospheric haze, tropospheric haze, and upper cloud). We have performed relative area photometry for the three ovals on the image series taken with the NSFCAM at IRTF (see Table 1) at wavelengths (pass bands indicated) 1.78 (0.035), 1.95 (0.039), 2.03 (0.041), and 2.30 (0.22) μm . The absolute photometry of HST NICMOS images at 1.87 (0.02) and 2.12 (0.02) μm was considered but unfortunately was not consistent with the photometry of WFPC2 and NSFCAM images. This is confirmed by our models that deviate substantially at these two wavelengths (see below). We used as a photometric reference the central

Table 4. Vortices Vertical Cloud Structure

| Feature | τ_1 | τ_2 | ω_0 | P_{TrHaze} (mbar) |
|--------------------------|-----------------|---------------|------------|----------------------------|
| GRS | 0.05 ± 0.02 | 7.5 ± 0.5 | 0.95 | 170 ± 30 |
| BA | 0.03 ± 0.01 | 1.7 ± 0.4 | 0.95 | 200 ± 40 |
| RO (before) ^a | 0.03 ± 0.01 | 2.0 ± 0.5 | 0.95 | 200 ± 60 |
| RO (after) ^b | 0.03 ± 0.02 | 1.5 ± 0.2 | 0.95 | 200 ± 60 |

^aBased on photometry before the RO interaction with the GRS.

^bBased on photometry on 10 July after the RO interaction with the GRS.

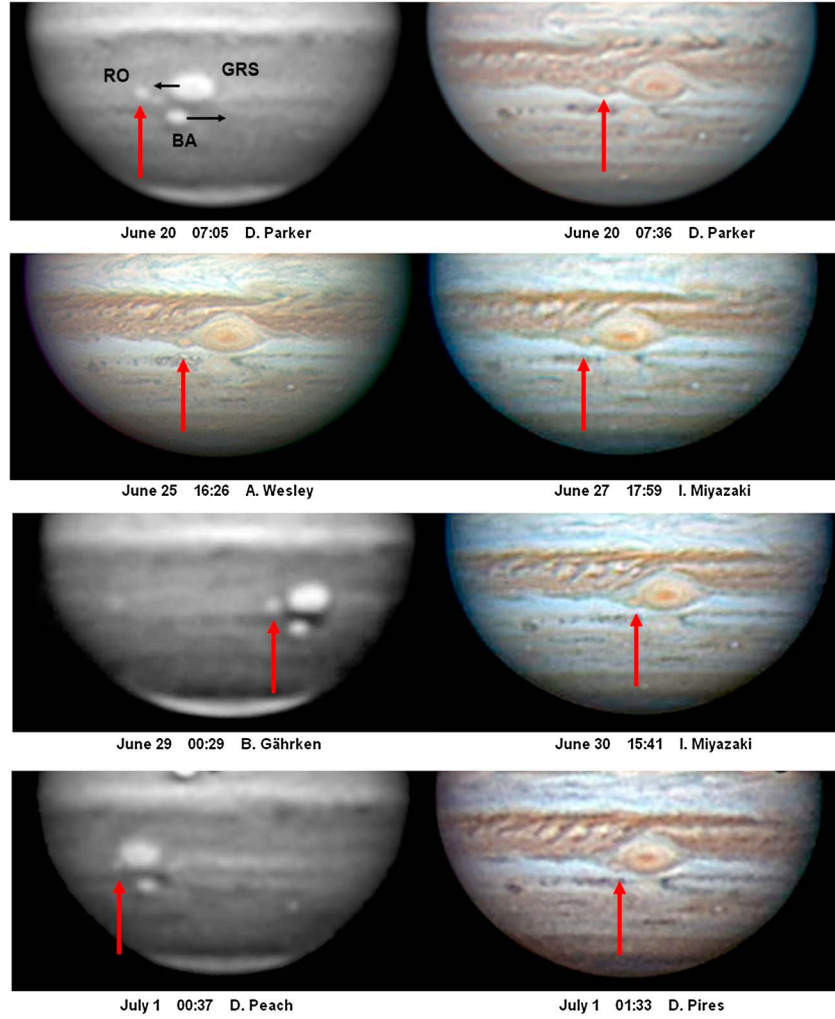


Figure 14.1. Approach sequence of RO relative to GRS and BA and their mutual interactions from IOPW images, starting on 20 June and ending on 15 July 2008. The color images are RGB composites, and the black and white images were obtained with an 890 nm methane band filter. The red arrow marks the position of oval RO. The GRS and BA are identified in the first image. Only the southern hemisphere is shown (south is up and east to the left). Dates and names of IOPW-PVOL and ALPO-Japan observers are indicated below each image.

area of the GRS. Relative to it, the brightness of BA and the RO ranged between 0.4 (in the deepest absorption band at $2.30\ \mu\text{m}$) and 0.7 (in the $1.78\ \mu\text{m}$ intermediate methane band).

[34] We have included for completeness an image obtained at $4.78\ \mu\text{m}$ in the thermal infrared (Figure 12g), a wavelength sensitive to the opacity of the clouds to the thermal emission from Jupiter. The GRS and BA show low thermal emission in their centers because of the high cloud opacity but higher emission in a low-opacity peripheral ring that results from a relatively low cloud opacity [e.g., Fletcher *et al.*, 2010; de Pater *et al.*, 2010b]. For the RO the situation is similar, with a high emission ring that corresponds well with the dark circular filament seen at the vortex periphery in the visible images (Figures 1 and 3). Details on the vortices opacity to Jovian thermal emission at $5\ \mu\text{m}$ are given in de Pater *et al.* [2010b].

6.2. Radiative Transfer Results

[35] We have used the reference model described in the previous section to perform simple radiative transfer

calculations to fit the photometric observations in the two spectral ranges. The aim is to gain some insight into the cloud top levels of the vortices during the interaction period, but we do not pretend to perform a full detailed study of their vertical structure. The radiative transfer code and procedure are described in Pérez-Hoyos *et al.*, 2005. The model has two haze layers with gas between them, overlying a dense cloud of isotropic scattering particles whose base is fixed at the ammonia condensation level (700 mbar). The free parameters are the optical depth (τ_1) of a physically thin topmost haze layer that we locate at an altitude level of 10 mbar, the optical depth (τ_2), and single-scattering albedo (ω_0) of the tropospheric haze layer and its top (minimum) pressure (P). The free parameters in this model are focused precisely on those parameters that were left unchanged (or were fixed) in de Pater *et al.* [2010b].

[36] We first computed the reflectivity at nadir viewing at 890 nm from pressures ranging from $P=100$ to $P=500$ mbar (1 mbar step) and particle optical thicknesses $\tau_2=5, 10, 50, 100, 500$, and 999 for two extreme cases:

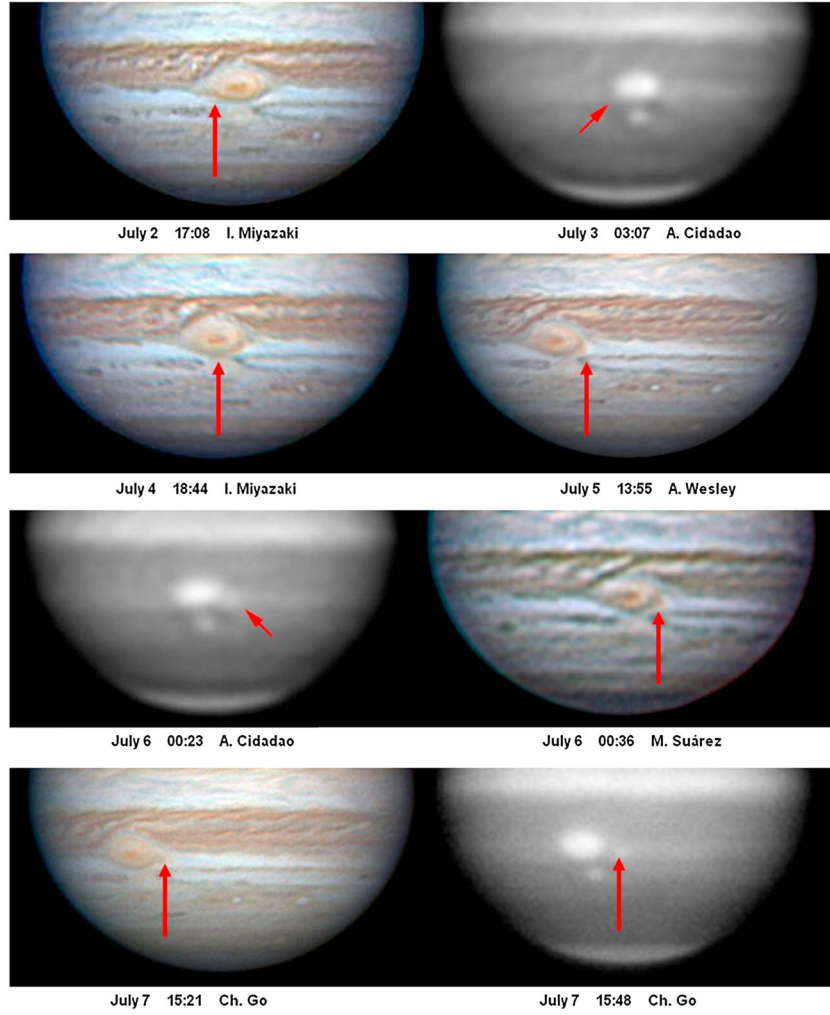


Figure 14.2

perfect scatterers ($\varpi_0 = 1.0$) and relatively absorbent particles ($\varpi_0 = 0.95$), which are commonly assumed values for the GRS [West *et al.*, 2004]. We distinguish arbitrarily between the two cases spanning the following ranges of optical depths: $\tau_2 = 5\text{--}10$ for the whole oval extent, a rather low value, and $\tau_2 = 50\text{--}1000$. This provided a framework of synthetic models with which we could compare the observed reflectivity for each case (Figure 13). Taking the first case scenario as the working frame in agreement with the results found for the GRS [West *et al.*, 2004, and references therein] and BA models [Pérez-Hoyos *et al.*, 2009; Strycker *et al.*, 2011], we determined the top pressure level, ϖ_0 , and τ_2 for the tropospheric haze for each vortex. Using the obtained values as a reference, we then fitted the near-infrared (NIR) reflectivity values to the model results to retrieve the optical depth of the stratospheric haze (τ_1), readjusting the values for the above parameters (Figure 13). The final results on our cloud structure model are given in Table 4, which in general agree with those presented by Strycker *et al.* [2011]. Comparison with results by de Pater *et al.* [2010b] is not so straightforward because of the differences in the modeling assumptions. However, our results are in good agreement with their assumption for the haze pressure top of 200 mbar. Optical thickness values are consistent with that work.

Complementarily, the UV images (see Figure 4) obtained with a filter at an effective wavelength of 255 nm are sensitive to particle absorption and to Rayleigh scattering by the gas (optical depth $\tau_g = 1$ at a pressure of 350 mbar) [West *et al.*, 2004; Strycker *et al.*, 2011]. Thus, the darkness of the ovals in the UV relative to their surroundings is mainly due to absorption produced by the particles in the high-altitude stratospheric haze. We conclude that the vertical structure of the hazes and upper clouds in the three ovals is very similar. The small differences in altitude and optical depth characterize their relative reflectivity.

7. RO-GRS-BA Dynamical Interaction

[37] The RO was nearly stationary in longitude (System III), whereas the GRS drifted west to increasing longitudes and BA east to decreasing longitudes (Table 2 and Figures 12 and 14). The GRS approached the RO from the west, and BA approached it from the east. Since the GRS dominated the scene due to its large size, we describe the RO and BA motions relative to it. Figure 14 shows images of the mutual approach sequence and the interaction of the three ovals at visual wavelengths. As described in detail in what follows, the interaction left the cloud morphology and

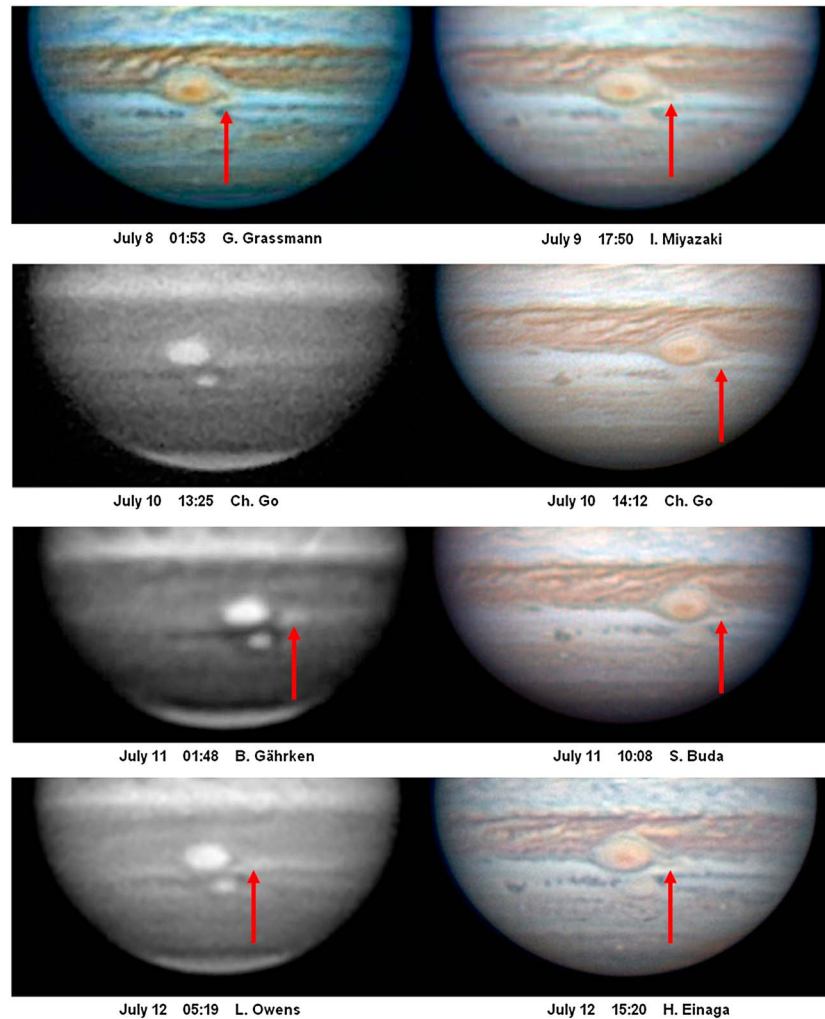


Figure 14.3

positions of the GRS and BA essentially unaltered, but it resulted in the destruction of the RO.

[38] About 250 individual position measurements of the center of the vortices (latitude and longitude) were performed in the 200 day interval from February to September 2008. In Figures 15 and 16 we show the longitude and latitude of the center of three ovals as a function of time. A first conclusion is that within the errors of our measurements, the GRS and BA did not change their positions when interacting with the RO. On the contrary, the RO interaction with the GRS not only altered its position but also destroyed the vortex. In Figure 17 we combined the previous data and mapped the motions (longitude-latitude) of the centers of the three ovals during the period of interaction. The RO entered the GRS on 28 June when arriving at its western edge and was advected southward by the anticyclonic peripheral flow of the GRS (see Figure 14.1-14.2). At this moment the RO increased its velocity slowly (relative to System III) from $\sim 1\text{--}2\text{ m s}^{-1}$ before the interaction to 5 m s^{-1} when it started, then the RO moved rapidly alongside the GRS southern edge while circulating along its periphery, accelerating until it reached a peak velocity of 55 m s^{-1} (Figure 18). This velocity is about half the value of the peak velocity typically found around the edge

of the GRS. The RO became elongated and shredded due to dynamical compression when it moved along the narrow channel formed between the GRS and BA when both vortices were close in longitude (Figure 14.2). Finally, the elongated RO reached the eastern edge of the GRS on 6–7 July as shown in the 890 nm methane band filter and in RGB color composites (Figures 14.3–14.4).

[39] The cloud morphology of the RO debris was well characterized on high-resolution images obtained at visible and near-infrared wavelengths. On 8 July, at visible wavelengths (Figure 15, inset), the RO consisted on a peripheral ring distorted from a circular shape and open on its western side (the one close to the GRS), with a less intense red color interior (as shown in section 5) and a small red residual remnant detached from its geometric center. On 9–10 July (Figure 19) the near-infrared images show in detail the RO cloud debris morphology at different altitude levels. Out of the methane and hydrogen strong absorption bands (Figure 19a), the RO showed a similar structure to that at visible wavelengths (compare with Figure 15, inset). Within the absorption bands at $2.12\text{ }\mu\text{m}$ and $2.30\text{ }\mu\text{m}$ (Figures 19b and 19c), the RO debris consisted on a bright compact cloud mass separated from the GRS but with a filamentary structure oriented

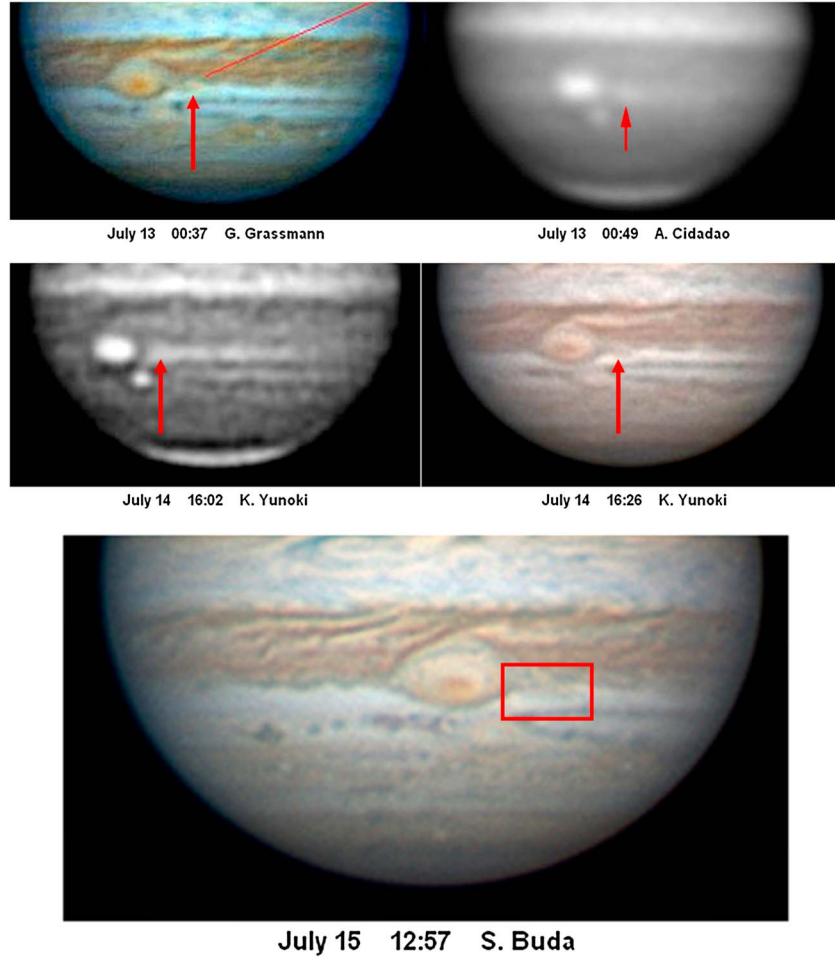


Figure 14.4

toward the peripheral flow of the GRS. Since these wavelengths sense the uppermost hazes of the vortices, it is clear that the RO cloud tops survived at about the same altitude level after the interaction. As shown in the previous section and in Table 4, the NIR photometry and radiative transfer modeling suggest that by 7 July, the RO tropospheric haze decreased its optical depth by about 25% relative to its value before interaction, without changing in altitude. Consequently, the interaction led to the destruction of the RO vortex structure and, at the same time, to its red color loss. By 25 July the RO cloud top residuals were dispersed by the meridional wind shears separating from the GRS (Figure 17d). Identification of the individual residuals in the near-infrared images by 22 August was very difficult and only a patchy bright band was visible (Figure 19e).

8. Numerical Simulations of the Vortices Interaction

[40] We carried out nonlinear numerical simulations of the observed characteristics of the mutual interaction between the GRS, BA, and the RO to infer the relative depth of the vortices and to assess the properties of Jupiter's cloudy weather layer in the region where the vortices reside. For this purpose, we used the EPIC code [Dowling *et al.*, 1998] as

we did in our previous studies of mergers and stability of Jovian vortices [Morales-Juberías *et al.*, 2003; Legarreta and Sánchez-Lavega, 2005]. We used potential vorticity (PV) to build horizontal maps to compare with the observed cloud field since PV is assumed to act as a passive tracer of the motions.

[41] In these simulations there are two groups of parameters that control the results. On the one hand, we have the properties of the vortices: size and latitude location of its center, wind velocity structure, and vertical extent. On the other, we must consider the properties of the Jovian weather layer: zonal wind meridional and vertical profiles, and vertical thermal structure (static stability or Brunt-Väisälä frequency). We vertically extended our model atmosphere across the lower stratosphere and upper cloudy troposphere (vertical range from 10 mbar to 7 bar of pressure).

[42] To model the velocity field of the three vortices, we added an ellipsoidal Gaussian perturbation to the Montgomery potential [Dowling *et al.*, 1998], which is the forcing term for the horizontal momentum equations in the EPIC isentropic coordinate model. When geostrophic balance is used to initialize the model, Montgomery potential horizontal gradients provide the adequate velocity profiles for the three vortices (see the details in García-Melendo *et al.* [2009]). By adjusting the shape parameters of the Gaussian perturbation we reproduce

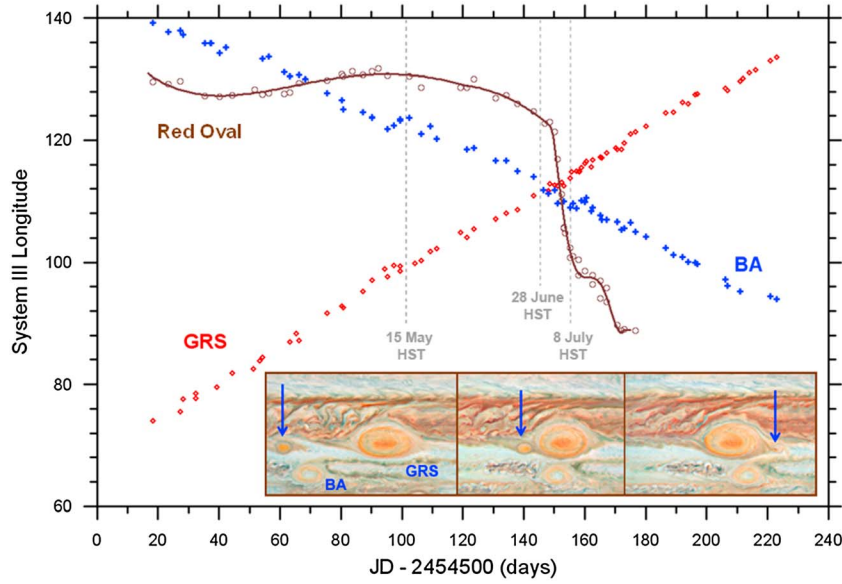


Figure 15. Long-term longitude drifts in System III of the three ovals RO, GRS, and BA. The reference 0 Julian day is for 2 February 2008 (reference dates for HST images are indicated). The inset shows HST color image composites of the area of interest around the GRS where RO is identified by the arrow for 15 May, 28 June, and 8 July (dates marked in the plot).

the particular velocity fields of the three vortices. For the GRS, we modeled the intense velocity ring at its periphery and its more stagnant interior [Legarreta and Sánchez-Lavega, 2005]. For the other two vortices, we assumed a more compact symmetric velocity distribution with velocity maxima close to the periphery. The geometrical parameters and the velocity describing the GRS and BA were also fixed to the experimental values. For the GRS we took -24° as the latitude position of its center and fixed its maximum tangential velocity at its periphery to $V_T = 115 \text{ m s}^{-1}$ [Sada et al., 1996; Asay-Davis et al., 2009].

We placed BA at latitude -33.3° and set its maximum tangential velocity at its periphery to 100 m s^{-1} [Hueso et al., 2009; Asay-Davis et al., 2009]. For the RO we placed the vortex between -24° and -27° latitudes and left as a free parameter the maximum tangential velocity at periphery testing values $V_T = 25, 50, \text{ and } 100 \text{ m s}^{-1}$. The vertical extent for BA and the GRS was fixed to $6H$, where $H = 20 \text{ km}$ is the average scale height, but this parameter was left free for the RO in order to assess the importance of its vertical extent. The vortices were centered at an altitude level of 680 mbar that corresponds

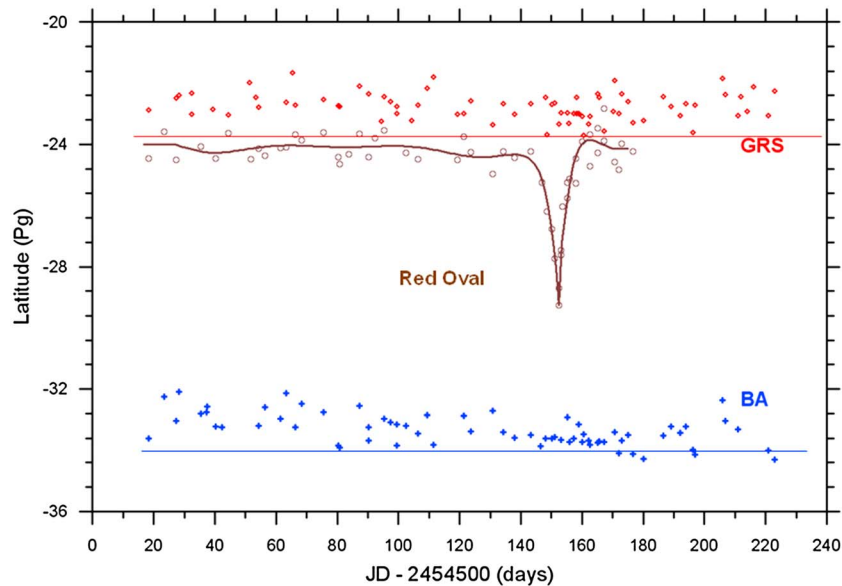


Figure 16. Same as Figure 15 but showing the long-term latitudinal position of the centers of the three ovals and their mean value from linear and polynomial fits.

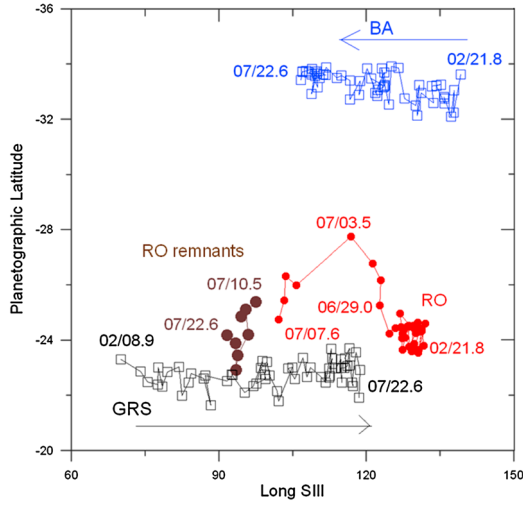


Figure 17. Motions in longitude and latitude of the centers of RO, GRS, and BA at the time of their interaction. The dates are indicated as month/day. For RO we distinguish two periods, the first when circling the GRS and the second when the RO remnant separated from the eastern edge of the GRS.

approximately to the location of the ammonia cloud. We found that the vertical extent of the RO is an essential ingredient to reproduce the GRS-RO interaction.

[43] For the background reference atmosphere (i. e., the weather layer) we tested different vertical structures (Figure 20) [see, e.g., *García-Melendo et al.*, 2005, 2009]. (1) For the zonal wind velocity, the following profiles were used: (a) The meridional profile $U_0(y)$ at cloud level is taken from *García-Melendo and Sánchez-Lavega* [2001]; (b) The vertical profile is divided in three parts. (i) Above the 60 mbar level in the stratosphere we assumed there is no wind, (ii) from 60 mbar to 680 mbar we take a profile derived in

previous studies $U(y, z) = U_0(y) \exp(-2.4z/H)$, which decays to zero at 60 mbar from the cloud tops, and (iii) from 680 mbar to 7 bar we left the profile as a free parameter with the winds increasing or decreasing linearly as characterized by different slopes m . (2) The vertical temperature profile was represented by the Brunt-Väisälä frequency $N(z)$, a measure of the static stability of the atmosphere. Above the 900 mbar level we took the profile from *Legarreta and Sánchez-Lavega* [2008]. Below the 900 mbar level we tested different $N(z)$ profiles, all constant in altitude but with different values across the cloudy layers (from ~ 1.1 bar down to 7 bar).

[44] From the numerical point of view, the EPIC simulations were run according to the following parameters: (a) The horizontal domain was a channel with a longitude length as long as 160° for our simulations and a latitude width of 40° with periodic walls in longitude; (b) The vertical domain extends from 10 mbar to 7 bar and was divided in eight isentropic layers; (c) The resolution was set between 0.15° and $0.31^\circ \text{ pixel}^{-1}$; (d) The integration time step was set at 60 s. Other parameters are similar to those of previous simulations [*Legarreta and Sánchez-Lavega*, 2008; *García-Melendo et al.*, 2009].

[45] We ran the first numerical experiments with the aim to fix the background reference atmosphere. As in our previous works, we determined the parameters $N(z)$ and $U(y, z)$ by studying the stability and motions of the vortices before their interaction. The motions of the individually simulated vortices were compared with the drift rates in longitude as measured for the GRS, BA, and the RO and shown in Figure 15. The best fit was found for profiles N0 and N1 shown in Figure 20 that are approximately constant between 1 and 7 bar with $N \sim 3-4 \times 10^{-3} \text{ s}^{-1}$. For the vertical dependence of the wind velocity we found that a constant profile $U(z) \sim U_0$ (case with slope m_3 in Figure 20) gave the best results, similar to previous results at other latitudes on deep winds [*Sánchez-Lavega et al.*, 2008].

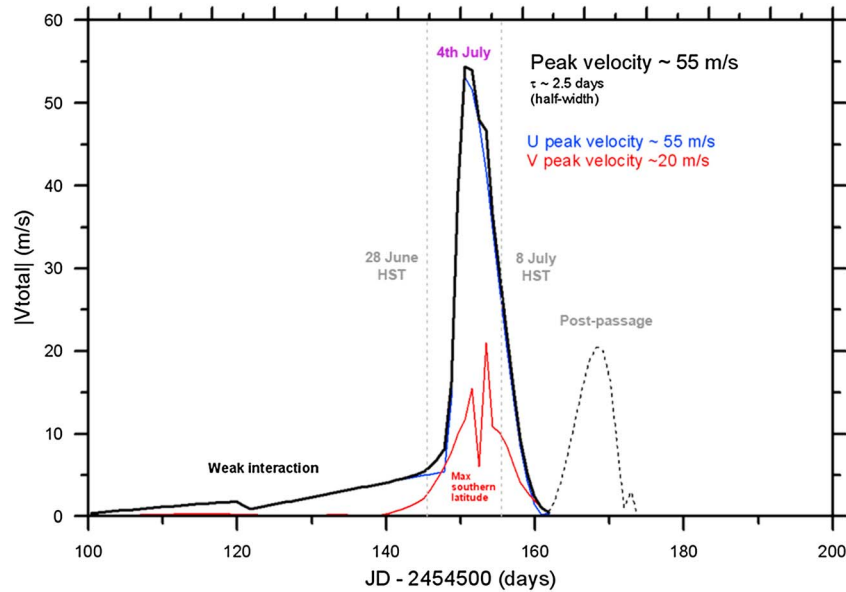


Figure 18. Velocity of the RO as a function of time before, during, and after its interaction with the GRS-BA. The zonal (blue line, u) and meridional (red line, v) velocity components and the module of the total velocity (black line, V) are indicated. Peak velocities are also indicated.

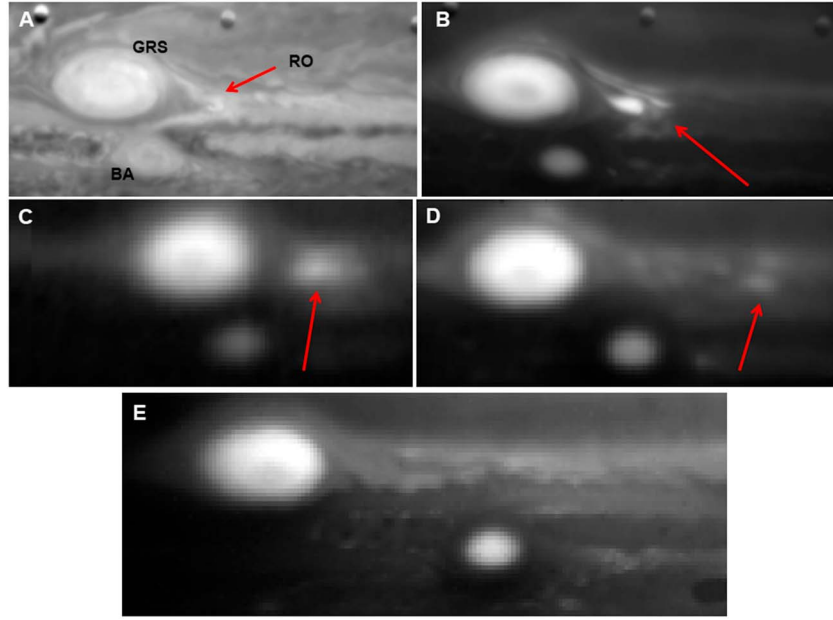


Figure 19. Images of the three anticyclones after their mutual interaction in the near infrared. They are identified with the RO debris marked in all image subsets by an arrow. They correspond to the following dates (2008) and wavelengths (in microns): (a) 9 July, HST-NICMOS, 1.87 μm ; (b) 9 July, HST-NICMOS, 2.12 μm (H_2 absorption band); (c) 10 July, IRTF-NSFCAM, 2.30 μm (CH_4 deep absorption band); (d) 25 July, UKIRT-UIST, 2.16 μm (CH_4 absorption band); and (e) 22 August, VLT-NACO, 2.166 μm (CH_4 absorption band).

[46] The next set of simulations was performed locating the three vortices in their respective latitudes, leaving the GRS fixed in longitude and placing BA and the RO far enough from the GRS to test their stability but, at the same time, drifting toward their mutual encounter (Figure 21). After about 100 days BA and the RO approach the GRS from its western side. The interaction between the GRS and the RO takes place around day 105. We found that the simulation of the RO destruction after flowing around the GRS southern rim is highly sensitive to the RO vortex strength and vertical extent. Only when the simulated RO is a weak ($V_T = 25 \text{ m s}^{-1}$)

and shallow vortex, (vertical extent = $2H$) are we able to reproduce reasonably well in the PV field the observed cloud morphology evolution (Figure 21). On the model, with RO centered at 0.68 bar, its base would be at about 1.8 bar. When the RO is simulated as a strong ($V_T = 100 \text{ m s}^{-1}$) and thick vortex like the GRS (vertical extent = $8H$), the RO-GRS interaction strongly modifies the PV field of the GRS so the PV patterns differ strongly from those observed. The RO simulated vortex that best reproduces the interaction has a strength consistent with our measurements. The simulations indicate that the GRS and the RO have a length to

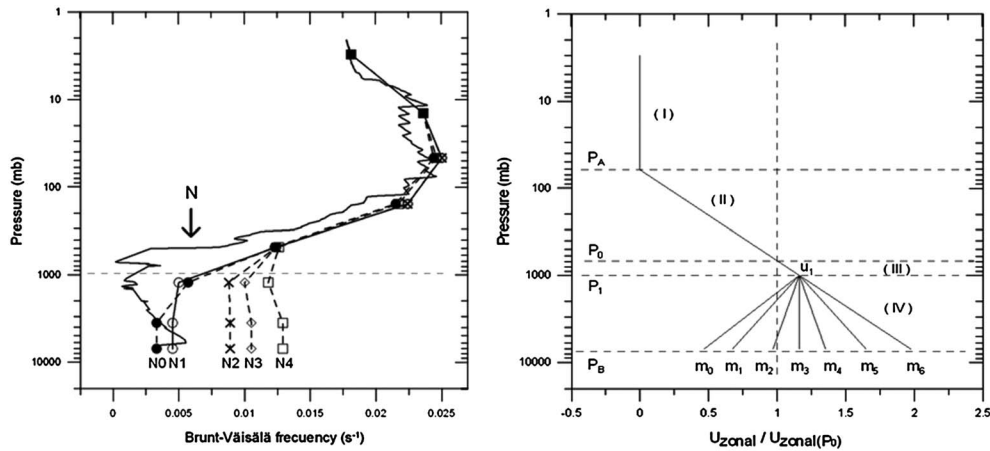


Figure 20. Vertical profiles for the Brunt-Väisälä frequency $N(z)$ and zonal wind $U(z)$ used in the EPIC numerical simulations of the vortices interaction. For $N(z)$, the vertical nominal profile is given by the continuous line N. We tested on EPIC the profiles N0 to N4 downward the altitude level of 900 mbar. For $U(z)$ we tested the series of profiles characterized by the different slopes m shown in region (III) downward the 680 mbar altitude level.

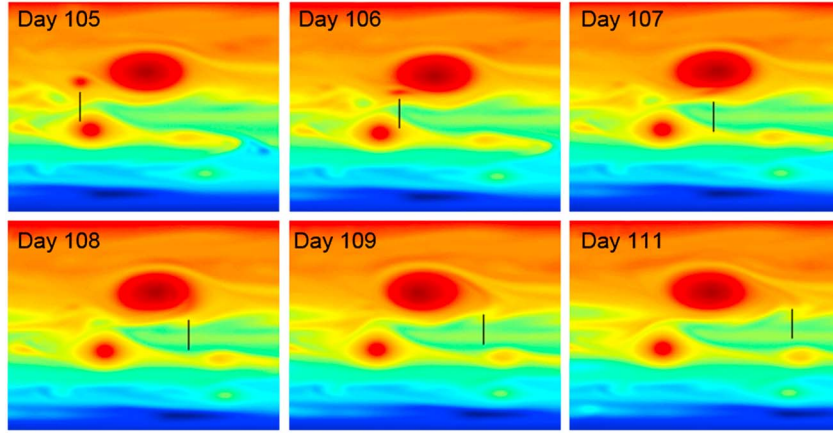


Figure 21. EPIC potential vorticity (PV) maps at the altitude level of 680 mbar (isentropic surface with potential temperature 187.5 K) from the numerical simulations showing the mutual interaction between the GRS and the RO, including also BA as a third oval in the area. The simulation day is indicated (at day 0 the three vortices totally separated) and the vertical bar marks the vortex RO. The PV color code ranges from -1.2 (blue, cyclonic) to $+8.6$ (red, anticyclonic) in units of $10^{-6} \text{ m}^2 \text{ K s}^{-1} \text{ kg}^{-1}$.

vertical extent ratio in the range $L_{\text{GRS}}/H_{\text{GRS}} \sim L_{\text{RO}}/H_{\text{RO}} \sim 100\text{--}120$ and a peak velocity ratio $V_T(\text{GRS})/V_T(\text{RO}) \sim 3\text{--}4$. However, these differences do not seem to have any effect on the red color of the two ovals.

9. Discussion and Conclusions

[47] Using relative reflectivity measurements, we have spectrally characterized the signature of the red color that stands out in color composite images of some anticyclonic vortices in the South Tropical and Temperate latitudes of Jupiter (ranging from latitudes -15° to -35°). The red signature manifests itself in the spectra as a broad absorption band between ~ 340 and 550 nm centered at $\sim 420 \text{ nm}$ (see also *Simon-Miller et al.* [2001a, 2001b, 2006] and *de Pater et al.* [2010b, 2011]). The red color is a permanent property, although temporally variable in its intensity, for the GRS and for an internal ring within BA, but it is rarely visible in the more frequent South Tropical Ovals (STrOs). It is striking to see that ovals that are similar in their dynamical properties and at the same latitude can show very different colors, from “white” (relatively flat spectra at visible wavelengths) to red. The best examples were the long-lived anticyclones BC, DE, and FA that for a period of about 60 years were “white” (they were nicknamed as “White Ovals”), but that after their merger to form BA [*Sánchez-Lavega et al.*, 1999, 2001] developed a red annular ring in its interior. The other example of color dichotomy is shown by the STrOs, most of them showing a white interior as the WTrOs, but with the Red Oval as a singular color case.

[48] Other red ovals have also been historically observed in the northern hemisphere at a symmetric latitude to that of the RO, i.e., at $19^\circ\text{--}20^\circ$ north during the Pioneer 10 flyby period in 1973 [*Swindell and Dose, 1974; Fimmel et al., 1980*], in ground-based photography [*Sánchez-Lavega and Quesada, 1988*] and in 1976 [*Beebe and Hockey, 1986; Sánchez-Lavega and Quesada, 1988*], and even northward at $41^\circ\text{N}\text{--}42^\circ\text{N}$, one of these vortices reaching a lifetime >14 years [*Rogers et al., 2010; de Pater et al., 2011*]. The similarity of these two northern stable vortices with the RO in their

color, vorticity (all are anticyclones), and location (close to a latitude where the profile has zero velocity), seems inescapable and points toward a same origin for the red color.

[49] The analysis of the reflectivity of the ovals GRS, BA, and RO in the $0.89\text{--}2.3 \mu\text{m}$ spectral region allowed us to constrain their vertical cloud structure in the upper troposphere and stratosphere. They showed very similar structure, with their tropospheric dense haze top located in all three cases at a similar altitude level of 200 mbar, i.e., above the surrounding clouds. For the RO this high-altitude haze prevailed after the destruction of the main vortex following its interaction with the GRS. These results are globally consistent with a similar analysis performed by *de Pater et al.* [2010b].

[50] The RO has a peripheral dark annulus (or ring) that encloses the red area with color-altitude properties similar to those of BA. These rings are usually seen in large vortices (those with a zonal length $>$ Rossby deformation radius $L_D \sim 2000\text{--}2500 \text{ km}$) and seem to contain an important part of the vortex circulation and vorticity [*Sada et al., 1996; Asay-Davis et al., 2009; Hueso et al., 2009; Sussman et al., 2010*]. We refer here to rings seen at visual wavelengths (reflected by clouds and hazes), not in thermal emission as was also discussed by *de Pater et al.* [2010b]. The motions of the few cloud features detected in the RO indicate that like the GRS, BA, and WTrOs, it is an anticyclonic vortex with tangential velocity $V_T \sim 50 \text{ m s}^{-1}$ and horizontal size $L_{\text{RO}}/L_{\text{GRS}} \sim 1/4$. However the four vortices have similar vorticities. One conclusion is that the color difference between WTrOs and the RO is not linked to two-dimensional vorticity or vortex strength. Numerical modeling of the interaction indicates that the relative vertical extent of both vortices is $H_{\text{RO}}/H_{\text{GRS}} \sim 1/4$. The model predicts a vertical to zonal length extent $D/L \sim 0.01$ which is of the same order to that found by *de Pater et al.* [2010b] in their proposed vortices models (~ 0.02). As the RO appears shallower than the GRS, one can infer that the red chromophore(s) is not linked to a deep bottom base of the oval. Finally, the RO ring was a coherent closed structure of the vortex confining the red chromophore within it, acting as a barrier against its dispersion or mixing with external material. The red color loss of the RO detected after the

interaction with the GRS was due to the dispersal of the haze particles when the dark ring opened and broke.

[51] The question of the origin of the red chromophore remains. A list of possible agent candidates has been proposed some time ago (see a summary in *West et al.* [1986]) and upper cloud chemistry and UV photolysis involving NH_3 and NH_4SH [Baines et al., 2004; Delitsky and Baines, 2007] and recently acetylene [Carlson et al., 2012], have also been suggested. In their study, *de Pater et al.* [2010b] suggest that the red chromophore is produced by descending air, originating in a secondary circulation above clouds that produces adiabatic heating on NH_3 ice exposing the red chromophores. Our numerical models do not require of such secondary circulation to explain the observed phenomena on the GRS-BA-RO mutual interaction. Here we discuss what we have learned about the red color in vortices from the RO study: (1) Red color prefers anticyclones to cyclones in most cases. (2) Red-colored features have high and dense top hazes (ovals are bright in the methane band images) as the GRS, the RO, and BA ring. This seems a necessary but insufficient condition for the presence of the red chromophore, since other anticyclones that are not red have upper hazes that are arguably just as high and dense, such as the White Ovals BC, DE, FA, and the WTrOs. (3) Red color does not depend on the vortex tangential velocity or the vorticity as diagnostics of oval dynamics [Sussman et al., 2010]. For the GRS, BA (ring), and the RO the vorticity at their peripheries was the same $\sim 2 \times 10^{-5} \text{ s}^{-1}$. However, there are anticyclones with the same vorticity that are not red (again the White Ovals and WTrO). (4) Tropical latitudes are favored for large anticyclones since large ovals form there (although they are not unique). (5) The red color does not depend on the vertical extent of the vortex below visible clouds (e.g., RO models indicate it was much shallower than the GRS). Thus, a deep “source” reservoir for red material that is transported upward inside the vortex could not be the case. This would appear to exclude the possibility that upwelling of sulfur-bearing molecules, for example, only takes place in anticyclones sufficiently deep to exhume H_2S or NH_4SH in sufficient abundance. (6) Color changes within anticyclones (e.g., reddening of the BA ring) do not appear to be related to vertical changes of the top altitude of the upper haze layer to which Charged Coupled Device (CCD) observations are sensitive [Pérez-Hoyos et al., 2009; Shetty and Marcus, 2010; Wong et al., 2011]. As a preliminary conclusion, the marked color differences from “white” to “red” seen in the anticyclones occur without notable changes in the vertical aerosol distribution or in the vortex wind field. This remains to be tested using longer-wavelength images characterizing BA between 2005 and 2006: (1) in the near infrared, which are sensitive to the highest haze properties, and (2) in the midinfrared, which are sensitive to temperatures and, thereby, winds.

[52] One possibility is that the red chromophore forms when background material (a compound or particles not always present) is entrained inside the vortex and transformed to red due to the vortex thermodynamic conditions, exposure to ultraviolet radiation, or to the mixing of two chemical compounds that react to form the red material. The red chromophore remains confined in the vortex by the peripheral ring that acts as a potential vorticity barrier against external mixing. A weakening of the PV barrier, favoring inward mixing of material or intrinsic internal changes in the vortex, leads to

temporal variability in the intensity of the red color [García-Melendo et al., 2009]. This is the case usually observed in the GRS that engulfs smaller vortices or other features formed for example during the large-scale SEB disturbances. This entrainment would need to be more effective in red-colored than white-colored anticyclones. This would allow, for example, particles to be lofted for a longer period and thereby satisfy both the necessary condition that particles be lofted to high altitudes, but a potentially sufficient condition that they remain there longer than in other anticyclones by virtue of their longevity. It remains now to identify the chemical nature of the red chromophore.

[53] **Acknowledgments.** This work was supported by the Spanish MICIIN project AYA2009-10701 and AYA2012-36666 with FEDER support, Grupos Gobierno Vasco IT464-07 and IT765-013, and UPV/EHU UFI11/55. We made use of computing facilities at CESCA in Barcelona with the help of MEC. Fletcher was supported by a Glasstone Fellowship at the University of Oxford during this research. Orton was supported by NASA through an award issued to the Jet Propulsion Laboratory, California Institute of Technology. This work is partly based on observations obtained from the data archive at the Space Telescope Science Institute. STScI is operated by the Association of Universities for Research in Astronomy, Inc., under NASA Contract NAS 5-26555. The Italian Telescopio Nazionale Galileo (TNG) is operated on the island of La Palma by the Fundación Galileo Galilei of the INAF (Istituto Nazionale di Astrofisica) at the Spanish Observatorio del Roque de los Muchachos of the Instituto de Astrofísica de Canarias. We acknowledge the support of Massimo Cecconi (INAF/Fundación Galileo Galilei, La Palma) in the observations with TNG and AdOpt. The IOPW and ALPO-Japan contributors are from the International Outer Planet Watch Team IOPW-PVOL: <http://www.pvol.ehu.es/pvol/index.jsp?action=iopw> and from ALPO-Japan (Association of Lunar and Planetary Observers) in Japan: <http://alpo-j.asahi-kawa-med.ac.jp/indexE.htm>.

References

- Asay-Davis, X., P. Marcus, M. Wong, and I. de Pater (2009), Jupiter's shrinking Great Red Spot and steady Oval BA: Velocity measurements with the Advection Corrected Correlation Image Velocimetry automated cloud tracking method, *Icarus*, **203**, 164–188.
- Baines, K. H., M. L. Delitsky, T. W. Momary, R. W. Carlson, and G. S. Orton (2004), Seeing red: Chromophores, clouds, and chemistry in Jupiter's Great Red Spot, *Bull. A. A. S.*, **36**, 1133.
- Banfield, D., P. J. Gierasch, M. Bell, E. Ustinov, A. P. Ingersoll, A. R. Vasavada, R. A. West, and M. J. S. Belton (1998), Jupiter's cloud structure from Galileo imaging data, *Icarus*, **135**, 230–250.
- Barrado-Izaguirre, N., J. F. Rojas, R. Hueso, A. Sánchez-Lavega, F. Colas, J. L. Dauvergne, D. Peach, and the IOPW Team (2013), Jupiter's zonal winds and their variability studied with small-size telescopes, *Astron. Astrophys.*, **554**, A74.
- Beebe, R. F., and T. A. Hockey (1986), A comparison of red spots in the atmosphere of Jupiter, *Icarus*, **67**, 96–105.
- Berrevoets C., B. DeClerq, T. George, D. Makolkina, P. Maxson, B. Pilz, P. Presnyakov, E. Roel, S. Weiller (2011), RegiStax 6 free processing software, <http://www.astronomie.be/registax/>.
- Borysow, A. (2002), Collision induced absorption coefficients of H_2 pairs at temperatures from 60 K to 1000 K, *Astron. Astrophys.*, **390**, 779–782.
- Cano, J.A. (1998), L.A.I.A. Laboratorio de Análisis de Imágenes Astronómicas. Grup d'Estudis Astronòmics, Barcelona (Spain).
- Carlson, R. W., K. H. Baines, M. S. Anderson, and G. Filacchione (2012), Chromophores from photolyzed ammonia reacting with acetylene: Application to Jupiter's Great Red Spot, *Bull. Am. Astron. Soc.*, **44**, 79.
- Chanover, N. J., D. M. Kuehn, D. Banfield, T. Momary, R. F. Beebe, K. H. Baines, P. D. Nicholson, A. A. Simon, and A. S. Murrell (1996), Absolute reflectivity spectra of Jupiter: 0.25–3.5 micrometers, *Icarus*, **121**, 351–360.
- Del Genio, A. D., R. K. Achterberg, K. H. Baines, F. M. Flasar, P. L. Read, A. Sánchez-Lavega, and A. P. Showman (2009), Saturn atmospheric structure and dynamics, in *Saturn After Cassini-Huygens*, edited by M. Dougherty, L. Esposito, and T. Krimigis, pp. 113–159, Springer-Verlag, Heidelberg.
- Delitsky, M. L., and K. H. Baines (2007), Jupiter's Great Red Spot: Cloud chemistry and chromophore formation, *Bull. Am. Astron. Soc.*, **39**, 444.
- de Pater, I., L. N. Fletcher, S. Pérez-Hoyos, H. B. Hammel, G. S. Orton, M. H. Wong, S. Luszcz-Cook, A. Sánchez-Lavega, and M. Boslough (2010a), A multi-wavelength study of the 2009 impact on Jupiter:

- Comparison of high-resolution images from Gemini, Keck and HST, *Icarus*, 210, 722–741.
- de Pater, I., M. H. Wong, P. S. Marcus, S. Luszcz-Cook, M. Ádámkóvics, A. Conrad, X. Asay-Davis, and C. Go (2010b), Persistent rings in and around Jupiter's anticyclones—Observations and theory, *Icarus*, 210, 742–762.
- de Pater, I., M. H. Wong, K. de Kleer, H. B. Hammel, M. Ádámkóvics, and A. Conrad (2011), Keck adaptive optics images of Jupiter's north polar cap and Northern Red Oval, *Icarus*, 213, 559–563.
- Dowling, T., A. S. Fisher, P. J. Gierasch, J. Harrington, R. P. LeBeau Jr., and C. M. Santori (1998), The Explicit Planetary Isentropic-Coordinate (EPIC) atmospheric model, *Icarus*, 132, 221–238.
- Dyudina, U. A., A. P. Ingersoll, G. E. Danielson, K. H. Baines, R. W. Carlson, and The Galileo NIMS, SSI Teams (2001), Interpretation of NIMS and SSI images on the Jovian cloud structure, *Icarus*, 150, 219–233.
- Fimmel, R. O., J. Van Allen, and E. Burgess (1980), *Pioneer, First to Jupiter, Saturn, and Beyond*, pp. 285, NASA SP-446, Washington D. C.
- Fletcher, L. N., et al. (2010), Thermal structure and composition of Jupiter's Great Red Spot from high-resolution thermal imaging, *Icarus*, 208, 306–328.
- García-Melendo, E., and A. Sánchez-Lavega (2001), A study of the stability of Jovian zonal winds from HST images: 1995–2000, *Icarus*, 152, 316–330.
- García-Melendo, E., A. Sánchez-Lavega, and T. Dowling (2005), Jupiter's 24°N highest speed-jet: Vertical structure deduced from nonlinear simulations of a large-amplitude natural disturbance, *Icarus*, 176, 272–282.
- García-Melendo, E., J. Legarreta, A. Sánchez-Lavega, R. Hueso, S. Pérez-Hoyos, J. González, J. M. Gómez-Forrellad, and the IOPW Team (2009), The Jovian anticyclone BA: I. Motions and interaction with the GRS from observations and non-linear simulations, *Icarus*, 203, 486–498.
- Hueso, R., J. Legarreta, E. García-Melendo, A. Sánchez-Lavega, and S. Pérez-Hoyos (2009), The Jovian anticyclone BA: II. Circulation and models of its interaction with the zonal jets, *Icarus*, 203, 499–515.
- Hueso, R., J. Legarreta, S. Pérez-Hoyos, J. F. Rojas, A. Sánchez-Lavega, and A. Morgado (2010), The International Outer Planets Watch atmospheres node database of giant planet images, *Planet. Space Sci.*, 58, 1152–1159.
- Ingersoll, A. P., T. E. Dowling, P. J. Gierasch, G. S. Orton, P. L. Read, A. Sanchez-Lavega, A. P. Showman, A. A. Simon-Miller, and A. R. Vasavada (2004), Dynamics of Jupiter's atmosphere, in *Jupiter: The Planet, Satellites and Magnetosphere*, edited by F. Bagenal, W. McKinnon, and T. Dowling, pp. 105–128, Cambridge Univ. Press, Cambridge, U. K.
- Karkoschka, E. (1998), Methane, ammonia, and temperature measurements of the Jovian planets and Titan from CCD-spectrophotometry, *Icarus*, 133, 134–146.
- Karkoschka, E., and A. M. Koekemoer (2002), WFPC2 flatfields with reduced noise and an anomaly of filter FQCH4N-D, in *The 2002 HST Calibration Workshop: Hubble After the Installation of the ACS and the NICMOS Cooling System*, edited by S. Arribas, A. Koekemoer, and B. Whitmore, pp. 315–324, Space Telescope Science Institute, Baltimore, MD.
- Law, N. M., C. D. Mackay, and J. E. Baldwin (2006), Lucky imaging: High angular resolution imaging in the visible from the ground, *Astron. Astrophys.*, 446, 739–745.
- Legarreta, J., and A. Sánchez-Lavega (2005), Jupiter's cyclones and anticyclones vorticity from voyager and Galileo images, *Icarus*, 174, 178–191.
- Legarreta, J., and A. Sánchez-Lavega (2008), Vertical structure of Jupiter's troposphere from nonlinear simulations of long-lived vortices, *Icarus*, 194, 184–201.
- Morales-Juberías, R., A. Sánchez-Lavega, J. Lecacheux, and F. Colas (2002), A comparative study of Jovian anticyclones properties from a six year (1994–2000) survey, *Icarus*, 157, 76–90.
- Morales-Juberías, R., A. Sánchez-Lavega, and T. Dowling (2003), EPIC simulations of the merger of Jupiter's White Ovals BE and FA: Altitude dependent behavior, *Icarus*, 166, 63–74.
- Pérez-Hoyos, S., A. Sánchez-Lavega, R. G. French, and J. F. Rojas (2005), Saturn's cloud structure and temporal evolution from ten years of Hubble Space Telescope images (1994–2003), *Icarus*, 176, 155–174.
- Pérez-Hoyos, S., A. Sanchez-Lavega, R. Hueso, E. García-Melendo, and J. Legarreta (2009), The Jovian anticyclone BA. III. Aerosol properties and color change, *Icarus*, 203, 516–530.
- Rogers, J. H. (1995), *The Giant Planet Jupiter*, pp. 418, Cambridge Univ. Press, Cambridge, U. K.
- Rogers, J. H., G. Adamoli, and H.-J. Mettig (2010), Jupiter's high-latitude storms: A little red spot tracked through a Jovian year, *J. Brit. Astron. Assoc.*, 121, 19–29.
- Sada, P. V., R. F. Beebe, and B. J. Conrath (1996), Comparison of the structure and dynamics of Jupiter's Great Red Spot between the Voyager 1 and 2 encounters, *Icarus*, 119, 311–335.
- Sánchez-Lavega, A., and J. A. Quesada (1988), Ground-based imaging of Jovian cloud morphologies and motions. II. The northern hemisphere from 1975 to 1985, *Icarus*, 76, 533–557.
- Sánchez-Lavega, A., and J. M. Gómez (1996), The South Equatorial Belt of Jupiter. I. Its life cycle, *Icarus*, 121, 1–17.
- Sánchez-Lavega, A., R. Hueso, J. Lecacheux, F. Colas, J. F. Rojas, J. M. Gómez, I. Miyazaki, and D. C. Parker (1998), Dynamics and Interaction between a large-scale vortex and the Great Red Spot in Jupiter, *Icarus*, 136, 14–26.
- Sánchez-Lavega, A., J. F. Rojas, R. Hueso, J. Lecacheux, F. Colas, J. R. Acarreta, I. Miyazaki, and D. C. Parker (1999), Interaction of Jovian White Ovals BC and DE in 1998 from Earth-based observations in the visual range, *Icarus*, 142, 116–124.
- Sánchez-Lavega, A. (2011), *An Introduction to Planetary Atmospheres*, pp. 587, CRC Press, Taylor & Francis, Boca Raton, Florida.
- Sánchez-Lavega, A., et al. (2001), The merger of two giant anticyclones in the atmosphere of Jupiter, *Icarus*, 149, 491–495.
- Sánchez-Lavega, A., et al. (2008), Depth of a strong Jovian jet from a planetary-scale disturbance driven by storms, *Nature*, 451, 437–440.
- Shetty, S., and P. S. Marcus (2010), Changes in Jupiter's Great Red Spot (1979–2006) and Oval BA (2000–006), *Icarus*, 210, 182–201.
- Shetty, S., X. Asay-Davis, and P. S. Marcus (2007), On the interaction of Jupiter's Great Red Spot and zonal jet streams, *J. Atmos. Sci.*, 64, 4432–4444.
- Simon-Miller, A. A., D. Banfield, and P. J. Gierasch (2001a), An HST study of Jovian chromophores, *Icarus*, 149, 94–106.
- Simon-Miller, A. A., D. Banfield, and P. J. Gierasch (2001b), Color and the vertical structure in Jupiter's belts, zones, and weather systems, *Icarus*, 154, 459–474.
- Simon-Miller, A. A., N. J. Chanover, G. S. Orton, M. Sussman, I. G. Tsavaris, and E. Karkoschka (2006), Jupiter's white oval turns red, *Icarus*, 185, 558–562.
- Smith, B. A. L. A., et al. (1979a), The Jupiter system through the eyes of Voyager 1, *Science*, 204, 951–972.
- Smith, B. A., et al. (1979b), The Galilean satellites and Jupiter: Voyager 2 imaging results, *Science*, 206, 927–950.
- Strycker, P. D., N. J. Chanover, A. A. Simon-Miller, D. Banfield, and P. J. Gierasch (2011), Jovian chromophore characteristics from multispectral HST images, *Icarus*, 215, 552–583.
- Sussman, M. G., N. J. Chanover, A. A. Simon-Miller, A. R. Vasavada, and R. F. Beebe (2010), Analysis of Jupiter's Oval BA: A streamlined approach, *Icarus*, 210, 202–210.
- Swindell, W., and L. R. Doose (1974), The imaging experiment in Pioneer 10, *J. Geophys. Res.*, 79, 3634–3644.
- Thompson, W. R. (1990), Global four-band spectral classification of Jupiter's clouds: Color/albedo units and trends, *Int. J. Supercomput. Appl.*, 4, 48–65.
- Vasavada, A. R., and A. P. Showman (2005), Jovian atmospheric dynamics: An update after Galileo and Cassini, *Rep. Prog. Phys.*, 68, 1935–1996.
- West, R. A., D. F. Strobel, and M. G. Tomasko (1986), Clouds, aerosols, and photochemistry in the Jovian atmosphere, *Icarus*, 65, 161–217.
- West, R. A., K. H. Baines, A. J. Friedson, D. Banfield, B. Ragert, and F. W. Taylor (2004), Jovian clouds and hazes, in *Jupiter: The Planet, Satellites and Magnetosphere*, edited by F. Bagenal, W. McKinnon, and T. Dowling, pp. 79–104, Cambridge Univ. Press, Cambridge, U. K.
- Wong, M. H., I. de Pater, X. Asay-Davis, P. S. Marcus, and C. Y. Go (2011), Vertical structure of Jupiter's oval BA before and after it reddened: What changed?, *Icarus*, 215, 211–225.